Performance-Driven Design of Carrier Phase Differential Navigation Frameworks With Megaconstellation LEO Satellites

JOE KHALIFE, Member, IEEE
University of California, Irvine, CA USA

ZAHER (ZAK) M. KASSAS, Senior Member, IEEE
The Ohio State University, Columbus, OH USA

A navigation framework with carrier phase differential measurements from megaconstellation low Earth orbit (LEO) satellite signals is developed. The measurement errors due to ephemeris errors and ionospheric and tropospheric delays are derived and the statistics of the dilution of precision is characterized. Moreover, the joint probability density function of the megaconstellation LEO satellites' azimuth and elevation angles is derived to 1) enable performance characterization of navigation frameworks with LEO satellites in a computationally efficient way and 2) facilitate parameter design, namely, the differential baseline, to meet desired performance requirements. The Starlink constellation is used as a specific LEO megaconstellation example to demonstrate the developed carrier phase differential LEO (CD-LEO) navigation framework. Simulation results are presented demonstrating the efficacy of the proposed CD-LEO framework for an unmanned aerial vehicle (UAV) navigating for 15.1 km in 300 s, while using signals from 44 Starlink satellites, achieving a 3-D position root mean squared error (RMSE) of 2.2 m and a 2-D RMSE of 32.4 cm. Experimental results are presented showing UAV navigating for 2.28 km in 2 min over Aliso Viejo, CA, USA, using exclusively signals from only two Orbcomm LEO satellites, achieving an unprecedented position RMSE of 14.8 m.

Manuscript received 9 July 2021; revised 17 February 2022 and 23 July 2022; accepted 1 November 2022. Date of publication 6 January 2023; date of current version 9 June 2023.

DOI. No. 10.1109/TAES.2023.3234521

Refereeing of this contribution was handled by J. Blanch.

This work was supported in part by the Office of Naval Research (ONR) under Grant N00014-19-1-2511, in part by the Air Force Office of Scientific Research (AFOSR) under Grant FA9550-22-1-0476, in part by the National Science Foundation (NSF) under Grant 1929965, and in part by the U.S. Department of Transportation (USDOT) under Grant 69A3552047138 for the CARMEN University Transportation Center (UTC)

Authors' addresses: Joe Khalife was with the Department of Mechanical and Aerospace Engineering, University of California, Irvine, CA 92697, USA, E-mail: (jjkhalife@gmail.com); Zaher (Zak) M. Kassas is with the Department of Electrical and Computer Engineering, The Ohio State University, Columbus, OH 43210, USA, E-mail: (zkassas@ieee.org). *(Corresponding author: Zaher (Zak) M. Kassas.)*

I. INTRODUCTION

The coming decade is slated to witness a space revolution with the launch of tens of thousands of low Earth orbit (LEO) satellites for broadband communication [1], [2]. The promise of utilizing LEO satellites for positioning, navigation, and timing (PNT) has been the subject of recent studies [3], [4], [5], [6], [7], [8], [9], [10], [11], [12], [13], [14], [15], [16], [17], [18]. While some of these studies call for tailoring the broadband protocol to support navigation capabilities [19], [20], other studies propose to exploit existing broadband LEO constellations for navigation in an opportunistic fashion [21], [22], [23], [24], [25], [26], [27]. The former studies allow for simpler receiver architectures and navigation algorithms. However, they require changes to existing infrastructure [28], the cost of which private companies, such as OneWeb, SpaceX, Boeing, and others, which are planning to aggregately launch tens of thousands of broadband Internet satellites into LEO, may not be willing to pay. Moreover, if the aforementioned companies agree to that additional cost, there will be no guarantees that they would not charge extra for "navigation services." In this case, exploiting broadband LEO satellite signals opportunistically for navigation becomes the more viable approach. An opportunistic approach also offers two additional advantages: 1) it maintains the privacy of the user, as only downlink LEO signals are utilized without communicating back with the LEO satellites and 2) it allows utilization of multiple constellations without being limited to only the subscription constellation. This article assesses opportunistic navigation with carrier phase differential measurements, also known as real-time kinematic (RTK), from broadband LEO satellite signals.

To address the limitations and vulnerabilities of global navigation satellite system (GNSS), opportunistic navigation has received significant attention over the past decade or so [29]. Opportunistic navigation is a paradigm that relies on exploiting ambient radio signal of opportunity (SOPs) for PNT. Besides LEO satellite signals, other SOPs include AM/FM radio [30], [31], [32], digital television [33], [34], and cellular [35], [36], [37], [38], [39], [40], [41], [42], [43], [44], with the latter showing the promise of a submeter-accurate navigation solution for unmanned aerial vehicles (UAVs) when carrier phase measurements from cellular signals are used [45], [46].

LEO satellites possess desirable attributes for positioning in GNSS-challenged environments [1], [2]: 1) they are around 20 times closer to Earth compared to GNSS satellites, which reside in medium Earth orbit (MEO), making their received signal power between 24 to 34-dBs higher than GNSS signals; 2) they will become abundant as tens of thousands of broadband Internet satellites are expected to be deployed into LEO; and 3) each broadband provider will

deploy broadband Internet satellites into unique constellations, transmitting at different frequency bands, making LEO satellite signals diverse in frequency and direction. While the ephemerides of LEO satellites are not as precisely known as those of GNSS satellites, estimates of the Keplerian elements parameterizing the orbits of these LEO satellites are made publicly available by the North American Aerospace Defense Command (NORAD) and are updated daily in the two-line element (TLE) files. Using TLEs and orbit determination algorithms (e.g., SGP4), the positions and velocities of these satellites can be estimated, albeit not precisely [47], [48], [49]. In addition, some of these broadband LEO satellites, such as Orbcomm satellites, are equipped with GPS receivers and broadcast their GPS solution to terrestrial receivers.

This article considers the problem of navigating exclusively with LEO satellite signals in environments where GNSS signals are unavailable or untrustworthy (e.g., in the presence of jamming or spoofing). To this end, there are several challenges that must be addressed. First, there are no publicly available receivers that can produce navigation observables from LEO satellite signals. Recent papers on navigation with LEO satellites have addressed this challenge for some of the existing constellations [21], [50], [51], [52], [53]. Second, existing navigation frameworks do not apply in a straight forward fashion to megaconstellation LEO satellites due to the unique error sources associated with megaconstellation LEO satellites. The literature on navigation with LEO satellites either 1) assumes that the orbit and clock errors of LEO satellites are precisely determined [54], [55], [56], [57], [58], 2) relies on TLEs [21], [50], [51], [52], 3) or simultaneously track LEO satellites and navigate [59], [60]. Obtaining precise LEO orbits and clocks requires additional infrastructure, the cost of which LEO broadband providers may not be willing to bare. Moreover, the error in the orbits obtained from the publicly available TLEs may be on the order of a few kilometers as the orbit is propagated way beyond the epoch at which the TLE file was generated. Blindly using the satellite positions obtained from the TLE files introduces significant errors in the measurement residuals [61]. Tracking the satellite orbits while navigating may reduce the error in satellite orbits; however, the augmented system becomes poorly estimable, especially for long period of navigation, i.e., 4 min or more [61]. An LEO carrier phase differential navigation framework was introduced in [62] to tackle the problem of large measurement errors due to LEO satellite orbit and clock errors. However, the framework was geared toward the Orbcomm constellation only. A third challenge is the unknown achievable navigation performance with megaconstellation LEO satellites. The navigation performance has been partially characterized in [62] and [63]. In [62], only the Orbcomm constellation was characterized, while none of the sources of errors were studied. In [63], stochastic models of the LEO satellite elevation and azimuth angles were developed to characterize the performance of LEO megaconstellations. However, the effect of satellite position errors on the measurement error were partially analyzed for a specific location, and ionospheric and tropospheric delays were not considered in the analysis.

The high level of precision of carrier phase measurements enables a submeter level navigation solution as has been demonstrated in GNSS [64] and cellular SOPs [45], [46]. This precision comes at the cost of added ambiguities that need to be resolved, for which the least-squares ambiguity decorrelation adjustment (LAMBDA) method can be employed [65]. Carrier phase differential measurements from LEO satellites have been used previously to accelerate integer ambiguity resolution in the case of GNSS [3], [4], [5], [66]. On one hand, the authors in [3] and [66] propose a method for resolving GNSS ambiguities by augmenting GNSS carrier phase measurements with ones taken from LEO satellites. On the other hand, Joerger et al. [4] and [5] discussed navigation and integrity monitoring with GNSS augmented with carrier phase measurements from Iridium satellites. Contrary to the aforementioned papers, this article does not assume that the rover can augment GNSS measurements with LEO measurements; thus, the rover is navigating exclusively with carrier phase differential measurements from LEO satellites. Moreover, the analysis in this article is not limited to one LEO constellation, but is generalized to multiple LEO megaconstellations.

Once the ambiguities are resolved, the rover can perform real-time positioning. As mentioned above, two major sources of error that have to be considered in the so-called carrier phase differential (CD)-LEO framework are 1) the error in the satellite positions obtained from the TLE files and 2) residual ionospheric and tropospheric delays as LEO satellites reside above the ionosphere and troposphere. Although the double-difference carrier phase measurements will cancel out most of satellite position errors and ionospheric and tropospheric delays, there will still be significant errors if the base and rover are "too far apart." These errors are too large to ignore if an accurate navigation solution is desired. This article characterizes this error and its statistics as a function of the differential baseline, from which the baseline can be designed to guarantee a desirable performance.

This article presents a study for carrier phase differential navigation with megaconstelation LEO satellites and considers the following scenario. A receiver onboard a "rover" with *unknown* states makes carrier phase measurements to LEO satellites, and a "base" station with known position in the vicinity of the rover makes carrier phase measurements to the same LEO satellites. One can form differential carrier phase measurements from base and rover measurements and solve for the rover's position as well as for the resulting ambiguities. Without any position priors, the rover cannot perform real-time positioning and must wait until there is enough change in satellite geometry to use a batch least-squares estimator to estimate its position and the integer ambiguities or use a dynamic estimator, such as an extended Kalman filter (EKF). The goal of the article is to develop a methodology for designing CD-LEO frameworks and analyzing their performance. Stochastic geometry models

have been used to characterize relevant metrics in terrestrial wireless communication systems [67]. Recent studies extended such models to LEO-based wireless communication systems [68], [69], [70], [71] to characterize coverage probabilities, interference, as well as Doppler spreads. This article aims to develop stochastic models for LEO satellite azimuth and elevation angles to characterize navigation performance metrics and error sources, namely, the dilution of precision (DOP), ephemeris errors, and atmospheric effects. Stochastic geometry models are an efficient alternative to full orbit simulations. Furthermore, they can still be used even when not enough information is known to simulate a given constellation. Stochastic geometry models can be used to calculate exact statistics of some performance metrics, either using numerical integration, or, although rarely simple, by deriving closed-form expressions in some instances. This article makes four contributions as follows.

1) First, a carrier phase differential (CD)-LEO navigation framework is developed for LEO satellite signals and the measurement residuals due to ephemeris, and ionospheric and tropospheric delays are derived.
2) Second, the probability density functions (pdfs) of megaconstellation LEO satellites' azimuth and elevation angles are used to characterize the cumulative density functions (cdfs) of the DOPs, namely, position DOP (PDOP), horizontal DOP (HDOP), and vertical DOP (VDOP).
3) Third, the statistics and cdfs of measurement residuals due to ephemeris errors and ionospheric and tropospheric delays are characterized as a function of the baseline. This study allows to design the system parameters to guarantee a desired performance, namely, the differential baseline.
4) Fourth, simulation and experimental results are presented showing a UAV localizing itself with LEO satellite signals using carrier phase differential measurements to an unprecedented level of accuracy. The simulation results show a UAV navigating for 15.1 km in 300 s, while using signals from 44 Starlink LEO satellites, achieving a 3-D position root mean squared error (RMSE) of 2.2 m and a 2-D RMSE of 32.4 cm. The experimental results show a UAV navigating for 2.28 km in 2 min over Aliso Viejo, CA, USA, using exclusively signals from only two Orbcomm LEO satellites, achieving a position RMSE of 14.8 m.

The rest of this article is organized as follows. Section II describes the measurement models used and the CD-LEO framework. Section III models the errors in the CD-LEO measurements due to ephemeris errors and ionospheric and tropospheric delays. Section IV derives the joint pdf of the megaconstellation LEO satellites' azimuth and elevation angles. Section V uses these models to characterize the performance of the CD-LEO framework and proposes a methodology to design system parameters to meet a desired performance. Section VI presents simulation results showing the potential of centimeter-accurate UAV navigation with fully deployed LEO magaconstellations. Section VII presents experimental results demonstrating a UAV navigating with CD-LEO measurements. Finally, Section VIII concludes this article.

II. MEASUREMENT MODELS AND CD-LEO FRAMEWORK DESCRIPTION

This section describes the measurement models and the CD-LEO framework used in the article. From here on out, a satellite will be referred to as a space vehicle (SV).

A. LEO Satellite Position Error

Let $\boldsymbol{r}_{\text{leo},l} \triangleq [x_{\text{leo},l}, y_{\text{leo},l}, z_{\text{leo},l}]^{\mathrm{T}}$ denote the lth LEO SV true position vector in the East–North–Up (ENU) frame. If the true LEO SV positions are not known, they may be estimated utilizing TLE files and orbit determination algorithms (e.g., SGP4), resulting with an estimate $\hat{\boldsymbol{r}}_{\text{leo},l}$. Denote the estimation error as $\tilde{\boldsymbol{r}}_{\text{leo},l} \triangleq \boldsymbol{r}_{\text{leo},l} - \hat{\boldsymbol{r}}_{\text{leo},l}$. Due to the large ephemeris errors in TLE files, $\|\tilde{\boldsymbol{r}}_{\text{leo},l}\|_2$ can be on the order of a few kilometers.

B. LEO Carrier Phase Observation Model

In this article, availability of carrier phase measurements from LEO SV signals is assumed. For example, the receiver proposed in [21] may be used to obtain carrier phase measurements from Orbcomm LEO SV signals and the one in [72] can be used for Starlink LEO SV signals. Note that Orbcomm LEO SVs transmit their SV ID. As such, data association for Orbcomm LEO SVs can be readily performed. However, little is known about Starlink LEO SV signals and data association must be performed. The problem of data association has been extensively studied in literature [73], [74] and its adaptation to the CD-LEO framework is left as future work. In the rest of the article, it is assumed that data association is performed perfectly. Note that since LEO satellite orbits are above the ionosphere, their signals will suffer from ionospheric and tropospheric delays. Let $\delta t^{(i)}_{\text{iono},l}(k)$ and $\delta t^{(i)}_{\text{trop},l}(k)$ denote the ionospheric and tropospheric delays from the lth LEO SV to the ith receiver at time-step k, respectively, where i denotes either the base B or the rover R. An estimate of the ionospheric and tropospheric delays, denoted $\hat{\delta} t^{(i)}_{\text{iono},l}(k)$ and $\hat{\delta} t^{(i)}_{\text{trop},l}(k)$, respectively, may be obtained using standard models [75]. After ionospheric and tropospheric delay correction, the carrier phase measurement $z^{(i)}_l(k)$ expressed in meters can be parameterized in terms of the receiver and LEO SV states as

$$z^{(i)}_l(k) = \left\|\boldsymbol{r}_{r,i} - \boldsymbol{r}_{\text{leo},l}(k)\right\|_2 + c\left[\delta t_{r,i}(k) - \delta t_{\text{leo},l}(k)\right] + \lambda_l N^{(i)}_l + c\tilde{\delta} t^{(i)}_{\text{trop},l}(k) + c\tilde{\delta} t^{(i)}_{\text{iono},l}(k) + v^{(i)}_l(k) \quad (1)$$

where $\boldsymbol{r}_{r,i} \triangleq [x_{r,i}, y_{r,i}, z_{r,i}]^{\mathrm{T}}$ is the ith receiver's position vector in ENU; c is the speed of light; $\delta t_{r,i}$ and $\delta t_{\text{leo},l}$ are the ith receiver's and lth LEO SV clock biases, respectively; $\tilde{\delta} t^{(i)}_{\text{iono},l} \triangleq \delta t^{(i)}_{\text{iono},l} - \hat{\delta} t^{(i)}_{\text{iono},l}$ and $\tilde{\delta} t^{(i)}_{\text{trop},l} \triangleq \delta t^{(i)}_{\text{trop},l} - \hat{\delta} t^{(i)}_{\text{trop},l}$ are the ionospheric and tropospheric delay errors, respectively; λ_l is the lth LEO SV signal's wavelength; $N^{(i)}_l$ is the carrier

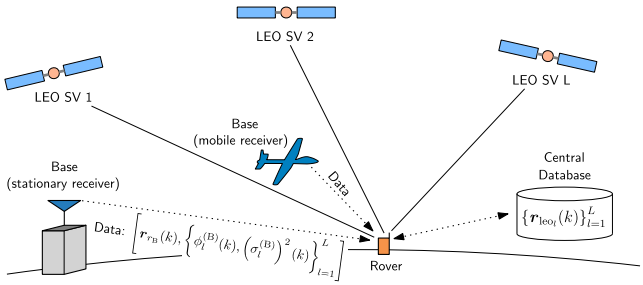

Fig. 1. Base/rover CD-LEO framework. The base receiver can be either (a) stationary or (ii) mobile (e.g., high-flying aerial vehicle).

phase ambiguity; and $v_l^{(i)}$ is the measurement noise, which is modeled as a discrete-time zero-mean white Gaussian sequence with variance $\left[\sigma_l^{(i)}(k)\right]^2$. It is assumed that $\left\{v_l^{(i)}\right\}_{l=1}^{L}$ are independent and identically distributed, but with different values of $\left[\sigma_l^{(i)}(k)\right]^2$.

C. CD-LEO Framework

The framework consists of a rover and a base receiver in an environment comprising L visible LEO SVs. The base receiver (B), is assumed to have knowledge of its own position state, e.g., 1) a stationary receiver deployed at a surveyed location or 2) a high-flying aerial vehicle with access to GNSS. The rover (R) does not have knowledge of its position. The base communicates its own position and carrier phase observables with the rover. The LEO SVs' positions are known through the TLE files and orbit determination software, or by decoding the transmitted ephemerides, if any. As such, one of two differential measurements may be used by the rover for navigating: 1) single difference or 2) double difference carrier phase measurements. Both of these measurements are discussed next. Fig. 1 illustrates the base/rover CD-LEO framework.

D. LEO Single Difference Carrier Phase Framework

In what follows, the objective is to estimate the rover's position using single difference carrier phase measurements. While these measurements eliminate the time-varying component of SV clock biases, the relative clock bias between the base and rover receivers as well as the carrier phase ambiguities cannot be resolved in the single difference measurements. As such, either 1) a precise prior is needed to estimate the initial ambiguities or 2) a dynamic estimator must be employed to estimate the ambiguities over time. The latter approach is adopted and an EKF is formulated to estimate the rover's position from single difference carrier phase measurements.

1) *LEO Single Difference Carrier Phase Observation Model:* First, define the single difference across receivers adjusted for the base-LEO SV range as

$$\begin{aligned} z_l^{(\mathrm{R,B})}(k) &\triangleq z_l^{(\mathrm{R})}(k) - z_l^{(\mathrm{B})}(k) + \left\|\boldsymbol{r}_{r,\mathrm{B}} - \hat{\boldsymbol{r}}_{\mathrm{leo},l}(k)\right\|_2 \\ &= \left\|\boldsymbol{r}_{r_\mathrm{R}} - \boldsymbol{r}_{\mathrm{leo},l}(k)\right\|_2 + c\delta t_r^{(\mathrm{R,B})}(k) + \lambda_l N_l^{(\mathrm{R,B})} \\ &\quad + c\tilde{\delta} t_{\mathrm{iono},l}^{(\mathrm{R,B})}(k) + c\tilde{\delta} t_{\mathrm{trop},l}^{(\mathrm{R,B})}(k) \\ &\quad - \tilde{r}_{\mathrm{leo},L}^{(\mathrm{B})}(k) + v_l^{(\mathrm{R,B})}(k) \end{aligned} \tag{2}$$

where

$$\begin{aligned} \delta t_r^{(\mathrm{R,B})}(k) &\triangleq \delta t_{r_\mathrm{R}}(k) - \delta t_{r_\mathrm{B}}(k) \\ \lambda_l N_l^{(\mathrm{R,B})} &\triangleq \lambda_l N_l^{(\mathrm{R})} - \lambda_l N_l^{(\mathrm{B})} \\ \tilde{\delta} t_{\mathrm{iono},l}^{(\mathrm{R,B})}(k) &\triangleq \tilde{\delta} t_{\mathrm{iono},l}^{(\mathrm{R})}(k) - \tilde{\delta} t_{\mathrm{iono},l}^{(\mathrm{B})}(k) \\ \tilde{\delta} t_{\mathrm{trop},l}^{(\mathrm{R,B})}(k) &\triangleq \tilde{\delta} t_{\mathrm{trop},l}^{(\mathrm{R})}(k) - \tilde{\delta} t_{\mathrm{trop},l}^{(\mathrm{B})}(k) \\ \tilde{r}_{\mathrm{leo},L}^{(\mathrm{B})}(k) &\triangleq \left\|\boldsymbol{r}_{r,\mathrm{B}} - \boldsymbol{r}_{\mathrm{leo},l}(k)\right\|_2 - \left\|\boldsymbol{r}_{r,\mathrm{B}} - \hat{\boldsymbol{r}}_{\mathrm{leo},l}(k)\right\|_2 \\ v_l^{(\mathrm{R,B})}(k) &\triangleq v_l^{(\mathrm{R})}(k) - v_l^{(\mathrm{B})}(k). \end{aligned}$$

Define $\tilde{\delta} t_{\mathrm{atmo},l}^{(\mathrm{R,B})}(k) \triangleq \tilde{\delta} t_{\mathrm{iono},l}^{(\mathrm{R,B})}(k) + \tilde{\delta} t_{\mathrm{trop},l}^{(\mathrm{R,B})}(k)$ as the overall delay in the lth single difference measurement due to atmospheric effects. Subsequently, $z_l^{(\mathrm{R,B})}(k)$ can be expressed as

$$\begin{aligned} z_l^{(\mathrm{R,B})}(k) &= h_l^{(\mathrm{R})}(k) + c\delta t_r^{(\mathrm{R,B})}(k) + \lambda_l N_l^{(\mathrm{R,B})} \\ &\quad + \tilde{r}_{\mathrm{leo},L}^{(\mathrm{R,B})}(k) + c\tilde{\delta} t_{\mathrm{atmo},l}^{(\mathrm{R,B})}(k) + v_l^{(\mathrm{R,B})}(k) \end{aligned} \tag{3}$$

where $h_l^{(\mathrm{R})}(k) \triangleq \|\boldsymbol{r}_{r_\mathrm{R}} - \hat{\boldsymbol{r}}_{\mathrm{leo},l}(k)\|_2$, $\tilde{r}_{\mathrm{leo},L}^{(\mathrm{R,B})}(k) \triangleq \tilde{r}_{\mathrm{leo},L}^{(\mathrm{R})}(k) - \tilde{r}_{\mathrm{leo},L}^{(\mathrm{B})}(k)$, and $\tilde{r}_{\mathrm{leo},L}^{(\mathrm{R})}(k) \triangleq \|\boldsymbol{r}_{r,\mathrm{R}} - \boldsymbol{r}_{\mathrm{leo},l}(k)\|_2 - \|\boldsymbol{r}_{r,\mathrm{R}} - \hat{\boldsymbol{r}}_{\mathrm{leo},l}(k)\|_2$. In vector form, the measurement equation becomes

$$\begin{aligned} \boldsymbol{z}(k) &= \boldsymbol{h}^{(\mathrm{R})}(k) + c\delta t_r^{(\mathrm{R,B})}(k)\mathbf{1}_L + \boldsymbol{A} \\ &\quad + \tilde{\boldsymbol{r}}_{\mathrm{leo}}^{(\mathrm{R,B})}(k) + c\tilde{\boldsymbol{\delta}} t_{\mathrm{atmo}}^{(\mathrm{R,B})}(k) + \boldsymbol{v}(k) \end{aligned} \tag{4}$$

where $\mathbf{1}_L$ is an $L \times 1$ vector of ones and

$$\begin{aligned} \boldsymbol{z}(k) &\triangleq \left[z_1^{(\mathrm{R,B})}(k), \ldots, z_L^{(\mathrm{R,B})}(k)\right]^{\mathrm{T}} \\ \boldsymbol{h}^{(\mathrm{R})}(k) &\triangleq \left[h_1^{(\mathrm{R})}(k), \ldots, h_L^{(\mathrm{R})}(k)\right]^{\mathrm{T}} \\ \boldsymbol{A} &\triangleq \left[\lambda_1 N_1^{(\mathrm{R,B})}, \ldots, \lambda_L N_L^{(\mathrm{R,B})}\right]^{\mathrm{T}} \\ \tilde{\boldsymbol{r}}_{\mathrm{leo}}^{(\mathrm{R,B})}(k) &\triangleq \left[\tilde{r}_{\mathrm{leo}_1}^{(\mathrm{R,B})}(k), \ldots, \tilde{r}_{\mathrm{leo},L}^{(\mathrm{R,B})}(k)\right]^{\mathrm{T}} \\ \tilde{\boldsymbol{\delta}} t_{\mathrm{atmo}}^{(\mathrm{R,B})}(k) &\triangleq \left[\tilde{\delta} t_{\mathrm{atmo},1}^{(\mathrm{R,B})}(k), \ldots, \tilde{\delta} t_{\mathrm{atmo},L}^{(\mathrm{R,B})}(k)\right]^{\mathrm{T}} \\ \boldsymbol{v}(k) &\triangleq \left[v_1^{(\mathrm{R,B})}(k), \ldots, v_L^{(\mathrm{R,B})}(k)\right]^{\mathrm{T}}. \end{aligned}$$

The covariance matrix of $\boldsymbol{v}(k)$ is given by $\mathbf{R}(k) \triangleq \mathrm{diag}\left[\left[\sigma_1^{(\mathrm{R,B})}(k)\right]^2, \ldots, \left[\sigma_L^{(\mathrm{R,B})}(k)\right]^2\right]$, where $\left[\sigma_l^{(\mathrm{R,B})}(k)\right]^2 \triangleq \left[\sigma_l^{(\mathrm{R})}(k)\right]^2 + \left[\sigma_l^{(\mathrm{B})}(k)\right]^2$.

2) *EKF Model:* In this framework, the rover may be stationary or mobile. Here, the position and velocity of the rover are estimated, along with the vector of ambiguities, yielding the state vector

$$\boldsymbol{x}_{\mathrm{EKF}}(k) = \left[\boldsymbol{r}_{r_\mathrm{R}}^{\mathrm{T}}(k), \quad \dot{\boldsymbol{r}}_{r_\mathrm{R}}^{\mathrm{T}}(k), \quad \boldsymbol{x}_{\mathrm{clk},r}^{(\mathrm{R,B})^{\mathrm{T}}}(k), \quad \boldsymbol{A}^{\mathrm{T}}\right]^{\mathrm{T}} \tag{5}$$

where $\boldsymbol{x}_{\mathrm{clk},r}^{(\mathrm{R,B})}(k) \triangleq \left[c\delta t_r^{(\mathrm{R,B})}(k), \quad c\dot{\delta} t_r^{(\mathrm{R,B})}(k)\right]^{\mathrm{T}}$ and $c\dot{\delta} t_r^{(\mathrm{R,B})}(k)$ is the relative drift between the rover and base clocks. Since the dynamics of the rover are not necessarily known, a simple, yet reasonable dynamical model is assumed for the rover's position and velocity,

namely, a velocity random walk model, which can be expressed as [76]

$$\boldsymbol{x}_{\rm pv}(k+1) = \mathbf{F}_{\rm pv}\boldsymbol{x}_{\rm pv}(k) + \boldsymbol{w}_{\rm pv}(k) \tag{6}$$

where $\boldsymbol{x}_{\rm pv}(k) \triangleq \left[\boldsymbol{r}_{r_{\rm R}}^{\rm T}(k),\ \dot{\boldsymbol{r}}_{r_{\rm R}}^{\rm T}(k)\right]^{\rm T}$, $\mathbf{F}_{\rm pv} \triangleq \begin{bmatrix} \mathbf{I}_{3\times3} & T\mathbf{I}_{3\times3} \\ \mathbf{0}_{3\times3} & \mathbf{I}_{3\times3} \end{bmatrix}$ is the state matrix, $\mathbf{I}_{n\times n}$ is the $n \times n$ identity matrix, $\mathbf{0}_{n\times n}$ is the $n \times n$ zero matrix, T is the sampling interval, and $\boldsymbol{w}_{\rm pv}(k)$ is the process noise, which is modeled as a zero-mean, white random vector with covariance $\mathbf{Q}_{\rm pv}$. In general, a clock error state $\boldsymbol{x}_{\rm clk} \triangleq [c\delta t, c\dot{\delta}t]^{\rm T}$ is modeled to evolve according to a standard double integrator driven by process noise [76], according to the dynamics model

$$\boldsymbol{x}_{\rm clk}(k+1) = \mathbf{F}_{\rm clk}\boldsymbol{x}_{\rm clk}(k) + \boldsymbol{w}_{\rm clk}(k) \tag{7}$$

where $\mathbf{F}_{\rm clk} \triangleq \begin{bmatrix} \mathbf{I}_{2\times2} & T\mathbf{I}_{2\times2} \\ \mathbf{0}_{2\times2} & \mathbf{I}_{2\times2} \end{bmatrix}$ and $\boldsymbol{w}_{\rm clk}(k)$ is the process noise, which is modeled as a zero-mean, white random vector with covariance $\mathbf{Q}_{\rm clk}$. Since $\boldsymbol{x}_{{\rm clk},r}^{\rm (R,B)}$ is the difference between the rover and base clock error states, then its dynamics will be similar to (7) except that its process noise covariance, denoted by $\mathbf{Q}_{{\rm clk},r}^{\rm (R,B)}$, will be the sum of the two process noise covariances, i.e.,

$$\mathbf{Q}_{{\rm clk},r}^{\rm (R,B)} = \mathbf{Q}_{{\rm clk},r}^{\rm (R)} + \mathbf{Q}_{{\rm clk},r}^{\rm (B)} \tag{8}$$

where $\mathbf{Q}_{{\rm clk},r}^{\rm (R)}$ and $\mathbf{Q}_{{\rm clk},r}^{\rm (B)}$ are the rover and base's clock error process noise covariances, respectively. Consequently, the overall dynamics of $\boldsymbol{x}_{\rm EKF}$ will be given by

$$\boldsymbol{x}_{\rm EKF}(k+1) = \mathbf{F}_{\rm EKF}\boldsymbol{x}_{\rm EKF}(k) + \boldsymbol{w}_{\rm EKF}(k) \tag{9}$$

where $\mathbf{F}_{\rm EKF} = {\rm diag}[\mathbf{F}_{\rm pv}, \mathbf{F}_{\rm clk}, \mathbf{I}_{L\times L}]$ and $\boldsymbol{w}_{\rm EKF}(k)$ is the overall process noise which is modeled as a zero-mean, white random vector with covariance $\mathbf{Q}_{\rm EKF} = {\rm diag}\left[\mathbf{Q}_{\rm pv}, \mathbf{Q}_{{\rm clk},r}^{\rm (R,B)}, \mathbf{0}_{L\times L}\right]$. Note that the block pertaining to the ambiguity vector is not exactly zero in the process noise covariance but is set to a small value $\epsilon\mathbf{I}$ to avoid numerical instabilities in the EKF [77]. The EKF can be readily implemented, with the measurement Jacobian given by

$$\mathbf{H}(k) = [\mathbf{G}(k) \quad \mathbf{1}_L \quad \mathbf{0}_L \quad \mathbf{I}] \tag{10}$$

where $\mathbf{G}(k)$ is the geometry matrix at time-step k, which can be parameterized by the SVs' azimuth and elevation angles $\{\phi_l\}_{l=1}^L$ and $\{\theta_l\}_{l=1}^L$, respectively, according to (11) equation shown at the bottom of this page.

E. LEO Double Difference Carrier Phase Framework

In what follows, the objective is to estimate the rover's position using double difference carrier phase measurements. While these measurements completely remove the dependency on clock biases, they have inherent ambiguities that must be resolved. Recall that $(L-1)$ measurements are obtained from L visible satellites [75], with one unknown ambiguity associated with each double difference measurement. Using only one set of carrier phase measurements with no *a priori* knowledge on the rover position results in an underdetermined system: $(L+2)$ unknowns (3 position states and $(L-1)$ ambiguities) with only $(L-1)$ measurements. Therefore, when no *a priori* information on the position of the rover is known, a batch weighted nonlinear least-squares (B-WNLS) over a window of K time-steps is employed to solve for the rover's position and ambiguities. The rover could either remain stationary or move during the batch window. Subsequently, the rover uses measurements collected at different times in a batch estimator, resulting in an overdetermined system [75]. The total number of measurements will be $K \times (L-1)$ in the batch window. If the rover remains stationary, the total number of unknowns will remain $(L+2)$. Otherwise, the number of unknowns becomes $(3\tilde{K} + L - 1)$: 3 position states at each time-step and $(L-1)$ ambiguities. The dimensions of the unknown parameters and the measurement vector set a necessary condition on K and L in order to obtain a solution. Once an estimate of the ambiguities is obtained, the rover position can be estimated in real-time using a point-solution weighted nonlinear least-squares (PS-WNLS) estimator. Both the B-WNLS and PS-WNLS estimate the rover's position from LEO double difference carrier phase measurements, which is described next.

1) *LEO Double Difference Carrier Phase Observation Model:* Without loss of generality, the first LEO SV is taken as the reference, yielding the double difference measurements

$$\begin{aligned}\bar{\boldsymbol{z}}(k) &\triangleq \mathbf{T}\boldsymbol{z}(k) \\ &= \bar{\boldsymbol{h}}^{\rm (R)}(k) + \bar{\boldsymbol{A}} + \bar{\tilde{\boldsymbol{r}}}_{\rm leo}^{\rm (R,B)}(k) + c\bar{\tilde{\boldsymbol{\delta}}}t_{\rm atmo}^{\rm (R,B)}(k) + \bar{\boldsymbol{v}}(k)\end{aligned} \tag{12}$$

where $\bar{\boldsymbol{h}}^{\rm (R)}(k) \triangleq \mathbf{T}\boldsymbol{h}^{\rm (R)}(k)$, $\bar{\boldsymbol{A}} \triangleq \mathbf{T}\boldsymbol{A}$, $\bar{\tilde{\boldsymbol{r}}}_{\rm leo}^{\rm (R,B)}(k) \triangleq \mathbf{T}\tilde{\boldsymbol{r}}_{\rm leo}^{\rm (R,B)}(k)$, $\bar{\boldsymbol{v}}(k) \triangleq \mathbf{T}\boldsymbol{v}(k)$, $\bar{\tilde{\boldsymbol{\delta}}}t_{\rm atmo}^{\rm (R,B)}(k) \triangleq \mathbf{T}\tilde{\boldsymbol{\delta}}t_{\rm atmo}^{\rm (R,B)}(k)$, and $\mathbf{T} \triangleq [-\mathbf{1}_{L-1}\ \ \mathbf{I}_{(L-1)\times(L-1)}]$ is the differencing matrix. Note that the covariance matrix of $\bar{\boldsymbol{v}}(k)$ is given by $\bar{\mathbf{R}}(k) = \mathbf{T}\mathbf{R}(k)\mathbf{T}^{\rm T}$. If $\lambda_l \neq \lambda_1$, then $\bar{\boldsymbol{A}}$ cannot be expressed as $\lambda\boldsymbol{N}$, where $\boldsymbol{N}$ is a vector of integers. If $\lambda_l = \lambda\ \forall\ l$, then $\bar{\boldsymbol{A}} = \lambda\boldsymbol{N}$ and the LAMBDA method is used to resolve the integer ambiguities.

2) *B-WNLS Solution:* If the rover remains stationary during the batch window, then the parameter to be estimated is given by

$$\boldsymbol{x}_{\rm stationary} \triangleq \left[\boldsymbol{r}_{r,{\rm R}}^{\rm T}(0), \bar{\boldsymbol{A}}^{\rm T}\right]^{\rm T}$$

$$\mathbf{G}(k) \triangleq -\begin{bmatrix} \cos[\theta_1(k)]\sin\left[\phi_1(k)\right] & \cos[\theta_1(k)]\cos\left[\phi_1(k)\right] & \sin[\theta_1(k)] \\ \vdots & \vdots & \vdots \\ \cos[\theta_L(k)]\sin\left[\phi_L(k)\right] & \cos[\theta_L(k)]\cos\left[\phi_L(k)\right] & \sin[\theta_L(k)] \end{bmatrix}. \tag{11}$$

otherwise, it is given by

$$\boldsymbol{x}_{\text{mobile}} \triangleq \left[\boldsymbol{r}_{r,\text{R}}^{\text{T}}(0), \ldots, \boldsymbol{r}_{r,\text{R}}^{\text{T}}(K-1), \bar{\boldsymbol{A}}^{\text{T}}\right]^{\text{T}}.$$

The parameter $\boldsymbol{x}_{\text{stationary}}$ or $\boldsymbol{x}_{\text{mobile}}$ are estimated from the collection of measurements from 0 to $(K-1)$ given by

$$\bar{\mathbf{z}}^K \triangleq \left[\bar{z}^{\text{T}}(0), \ldots, \bar{z}^{\text{T}}(K-1)\right]^{\text{T}}$$

to yield an estimate $\hat{\boldsymbol{x}}_{\text{stationary}}$ or $\hat{\boldsymbol{x}}_{\text{mobile}}$, respectively. Let $\hat{\bar{\boldsymbol{A}}}$ denote the estimate of $\bar{\boldsymbol{A}}$. For a mobile receiver, the estimation error covariance $\mathbf{Q}_A$ associated with $\hat{\bar{\boldsymbol{A}}}$ is given by

$$\mathbf{Q}_A = \left(\sum_{k=0}^{K-1} \mathbf{Y}_k^{\frac{1}{2}} \boldsymbol{\Omega}_k \mathbf{Y}_k^{\frac{1}{2}}\right)^{-1}$$

where $\mathbf{Y}_k^{\frac{1}{2}}$ is a square-root of $\mathbf{Y}_k \triangleq \bar{\mathbf{R}}^{-1}(k)$, and

$$\boldsymbol{\Omega}_k \triangleq \mathbf{I}_{(L-1)\times(L-1)} - \boldsymbol{\Psi}_k$$
$$\boldsymbol{\Psi}_k \triangleq \mathbf{Y}_k^{\frac{1}{2}} \mathbf{T}\mathbf{G}(k) \left[\mathbf{G}^{\text{T}}(k)\mathbf{T}^{\text{T}}\mathbf{Y}_k\mathbf{T}\mathbf{G}(k)\right]^{-1} \mathbf{G}^{\text{T}}(k)\mathbf{T}^{\text{T}}\mathbf{Y}_k^{\frac{1}{2}}$$

where $\mathbf{G}(k)$ is given in (11).

REMARK 1 In this article, the well-known LAMBDA method is adopted to resolve integer ambiguities. However, the CD-LEO framework may be implemented with a different integer ambiguity resolution method. Regardless of the resolution method used, the integers may not be resolved properly, especially that many of the LEO megaconstellations of interest will be transmitting in the Ka band and above. Since the wavelength is very small (3 cm or less), the difference between the float and integer solution will also be very small. In this case, errors due to uncertainty in the ephemeris would dominate. This source of error is one of the main sources characterized in this article. Nevertheless, the methodology developed in this article can be readily extended to study the effect of the integer resolution algorithm and the batch window size on the navigation performance of the CD-LEO framework and is left as future work.

3) *PS-WNLS Solution:* After resolving the ambiguities, a point solution for the rover position can be computed at each time-step. Let $\check{\boldsymbol{N}}$ denote the integer estimates of $\boldsymbol{N}$. Hence, the double difference measurement vector adjusted for the integer ambiguities expressed as

$$\bar{z}_f(k) \triangleq \bar{z}(k) - \lambda\check{\boldsymbol{N}} = \bar{\boldsymbol{h}}, \text{R}(k) + \lambda\tilde{\boldsymbol{N}} + \bar{\tilde{\boldsymbol{r}}}_{\text{leo}}^{(\text{R,B})}(k) + \bar{\boldsymbol{v}}(k) \tag{13}$$

where $\tilde{\boldsymbol{N}} \triangleq \boldsymbol{N} - \check{\boldsymbol{N}}$ is the integer ambiguity error. The rover uses $\bar{z}_f(k)$ to solve for $\boldsymbol{r}_{r_{\text{R}}}(k)$ in a PS-WNLS. For small measurement noise variances, which is typically the case for high-frequency carriers, the positioning performance heavily depends on $\bar{\tilde{\boldsymbol{r}}}_{\text{leo}}^{(\text{R,B})}(k)$, which is characterized in Section V.

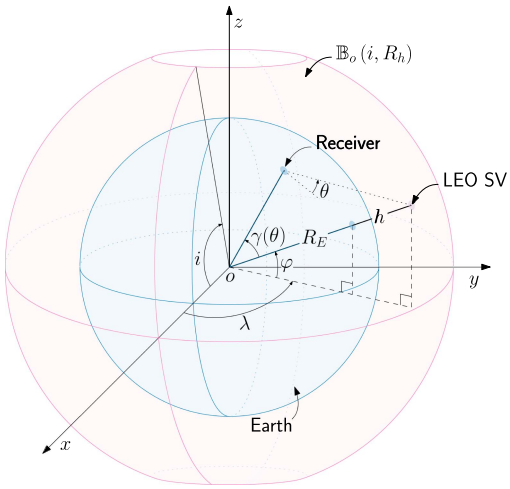

Fig. 2. LEO SV-to-receiver geometry. The subscripts j and l are omitted for simplicity.

III. LEO MEGACONSTELLATION AND ERROR MODELS

This section describes the LEO megaconstellation orbit model as well as models of ephemeris and ambiguity resolution errors.

A. LEO Megaconstellation Orbit Model

Consider a LEO megaconstellation composed of J LEO constellations of L_j SVs each, where $j = 1, \ldots, J$. The total number of SVs in the megaconstellation is given by

$$L = \sum_{j=1}^{J} L_j. \tag{14}$$

The orbit of a LEO SV belonging to constellation j is defined by its inclination angle i_j and orbital altitude h_j. Define the normalized orbital radius

$$\alpha_j \triangleq 1 + \frac{h_j}{R_E} \tag{15}$$

where R_E is the average radius of the Earth, which is assumed to be spherical. The surface over which the LEO SV can exist is defined as $\mathbb{B}_o(i_j, R_{h_j})$, which is a capless sphere of radius $R_{h_j} \triangleq \alpha_j R_E$, as shown in Fig. 2. The subsequent analysis can be done independently for different LEO constellation; hence, the subscript j will be dropped for simplicity of notation. Let ϕ_l and θ_l denote the azimuth and elevation angles, respectively, of the lth LEO SV. These angles are specific to a receiver location given by longitude λ_0 and latitude φ_0. Moreover, let $\gamma(\theta_l)$ denote the angle between the LEO SV and receiver position vectors. Using the law of sines, $\gamma(\theta_l)$ can be expressed as

$$\gamma(\theta_l) = \cos^{-1}\left[\frac{1}{\alpha}\cos\theta_l\right] - \theta_l. \tag{16}$$

The constellation parameters are obtained from the proposed Starlink constellation in [78] and are summarized in Table I.

TABLE I
Starlink Orbital Configuration

Parameter	LEO constellation				
Satellites per altitude	1600	1600	400	375	450
Altitude (km)	1150	1110	1130	1275	1325
Inclination (°)	53	53.8	74	81	70

B. Measurement Errors Due to Ephemeris Errors

Recall that the SV positions are obtained by nonprecise ephemerides. The effect of the estimated SV position error onto the CD-LEO measurement is first characterized as a function of the SV elevation angle. Next, the pdf of the elevation angle derived in Section IV is used to obtain the cdf of the measurement error due to ephemeris errors. A first-order Taylor series expansion around $\hat{\boldsymbol{r}}_{\text{leo},l}$ yields

$$\left\|\boldsymbol{r}_{r,i}-\boldsymbol{r}_{\text{leo},l}\right\|_2 \approx \left\|\boldsymbol{r}_{r,i}-\hat{\boldsymbol{r}}_{\text{leo},l}\right\|_2 + \boldsymbol{h}_{i,l}^{\mathsf{T}}\tilde{\boldsymbol{r}}_{\text{leo},l}^{(i)} \tag{17}$$

where $\boldsymbol{h}_{i,l}$ is the unit line-of-sight vector between the lth LEO SV and the ith receiver and $\tilde{\boldsymbol{r}}_{\text{leo},l}^{(i)}$ is the lth LEO SV's position error vector expressed in the ith receiver's ENU frame. A first-order Taylor series expansion around $\boldsymbol{h}_{\text{B},l}$ yields

$$\boldsymbol{h}_{\text{R},l} \approx \boldsymbol{h}_{\text{B},l} + \frac{1}{\left\|\boldsymbol{r}_{r,\text{B}}-\hat{\boldsymbol{r}}_{\text{leo},l}\right\|_2}\left(\mathbf{I}-\boldsymbol{h}_{\text{B},l}\boldsymbol{h}_{\text{B},l}^{\mathsf{T}}\right)\Delta\boldsymbol{r}_b \tag{18}$$

where $\Delta\boldsymbol{r}_b$ is the baseline vector between the base and the rover. Subsequently, the residual due to SV position errors can be expressed as

$$\begin{aligned}\tilde{r}_{\text{leo},l}^{(\text{R,B})} =\ & \left\|\boldsymbol{r}_{r,\text{R}}-\boldsymbol{r}_{\text{leo},l}\right\|_2 - \left\|\boldsymbol{r}_{r,\text{B}}-\boldsymbol{r}_{\text{leo},l}\right\|_2 \\ & - \left\|\boldsymbol{r}_{r,\text{R}}-\hat{\boldsymbol{r}}_{\text{leo},l}\right\|_2 + \left\|\boldsymbol{r}_{r,\text{B}}-\hat{\boldsymbol{r}}_{\text{leo},l}\right\|_2 \\ \Rightarrow \tilde{r}_{\text{leo},l}^{(\text{R,B})} \approx & \frac{\left(\boldsymbol{\Xi}_l\tilde{\boldsymbol{r}}_{\text{leo},l}^{(B)}\right)^{\mathsf{T}}\left(\boldsymbol{\Xi}_l\Delta\boldsymbol{r}_b\right)}{d_l^{(\text{B})}}\end{aligned} \tag{19}$$

where $\boldsymbol{\Xi}_l \triangleq (\mathbf{I}-\boldsymbol{h}_{\text{B},l}\boldsymbol{h}_{\text{B},l}^{\mathsf{T}})$ and $d_l^{(\text{B})} \triangleq \|\boldsymbol{r}_{r,\text{B}}-\hat{\boldsymbol{r}}_{\text{leo},l}\|_2$. Using the law of sines and (16), $d_l^{(i)}$ can be expressed as

$$d_l^{(i)} = R_E\left(\sqrt{\alpha^2-\cos^2\theta_l^{(i)}}-\sin\theta_l^{(i)}\right) \tag{20}$$

where $\theta_l^{(i)}$ denotes the lth LEO SV's elevation angle in the ith receiver's coordinate frame. The residual in (19) can be interpreted as the dot product between the baseline projected onto the range-space of $\boldsymbol{\Xi}_l$, denoted $\mathcal{R}(\boldsymbol{\Xi}_l)$, and the SV position error vector also projected onto $\mathcal{R}(\boldsymbol{\Xi}_l)$, as shown in Fig. 3(a). Practically, the rover can be assumed to be on the base's local plane East–North (EN) plane, i.e., its elevation angle with respect to the base is zero. Moreover, let $\omega_{\text{R}}^{(\text{B})}$ denote the rover's azimuth angle with respect to the base, as shown in Fig. 3(b). As such, the baseline can be parameterized as

$$\Delta\boldsymbol{r}_b = \Delta r_b\boldsymbol{u}_{\text{R}}^{(\text{B})} \tag{21}$$

where $\boldsymbol{u}_{\text{R}}^{(\text{B})} \triangleq [\sin\omega_{\text{R}}^{(\text{B})}, \cos\omega_{\text{R}}^{(\text{B})}, 0]^{\mathsf{T}}$ is a unit vector representing the baseline direction and Δr_b is the baseline magnitude.

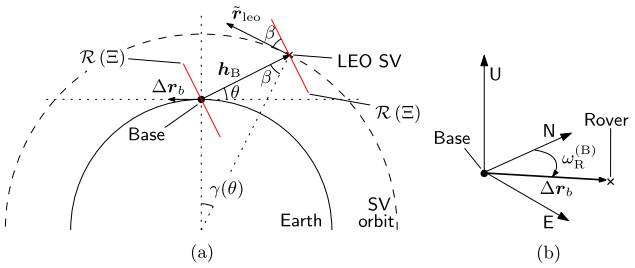

Fig. 3. Baseline-to-SV geometry. The subscript l was omitted for simplicity. The red lines show the range-space of $\boldsymbol{\Xi}$, denoted by $\mathcal{R}(\boldsymbol{\Xi})$, which is orthogonal to the unit line-of-sight vector $\boldsymbol{h}_{\text{B}}$.

Moreover, let $\psi_l^{(\text{B})}$ denote the orientation of the LEO SV's ground track in the base's ENU frame. As such, the LEO SV's position error vector may be expressed in the base's ENU frame as

$$\tilde{\boldsymbol{r}}_{\text{leo},L}^{(\text{B})} = e_{\text{leo},L}\boldsymbol{u}_{\text{leo},L}^{(\text{B})} \tag{22}$$

where $e_{\text{leo},L}$ is the magnitude of the SV position error and $\boldsymbol{u}_{\text{leo},L}^{(\text{B})}$ is the unit direction vector of the SV error in the base's ENU frame. Using (16) and the geometry in Fig. 3, one can show that $\boldsymbol{u}_{\text{leo},L}^{(\text{B})}$ can be expressed as

$$\begin{aligned}\boldsymbol{u}_{\text{leo},L}^{(\text{B})} \triangleq \frac{1}{\alpha}\Big[&\sin\psi_l^{(\text{B})}\cos\theta_l^{(\text{B})}, \cos\psi_l^{(\text{B})}\cos\theta_l^{(\text{B})}, \\ &\sqrt{\alpha^2-\cos^2\theta_l^{(\text{B})}}\Big]^{\mathsf{T}}.\end{aligned} \tag{23}$$

Using (19)–(23), the measurement residual due to SV position error can be expressed as

$$\tilde{r}_{\text{leo},l}^{(\text{R,B})} = f\left(\theta_l^{(\text{B})}, \phi_l^{(\text{B})}, \omega^{(\text{B})}, \text{R}, \psi_l^{(\text{B})}, \alpha\right)\frac{\Delta r_b\cdot e_{\text{leo},L}}{R_E} \tag{24}$$

where

$$\begin{aligned}f(\theta,\phi,\omega,\psi,\alpha) \triangleq\ & \frac{\cos\theta}{\alpha\left(\sqrt{\alpha^2-\cos^2\theta}-\sin\theta\right)} \\ & \cdot\Big[\cos(\psi-\omega)-\cos(\psi-\phi)\cos\theta \\ & -\alpha\cos(\omega-\phi)-\frac{\sin\theta\sqrt{\alpha^2-\cos^2\theta}}{\cos\theta}\Big].\end{aligned} \tag{25}$$

While (24) shows the mapping between SV position error and measurement residual, it is worth looking at an upper bound of the residual magnitude for worst case scenario analysis. It can be seen from Fig. 3(a) that the magnitude of $\tilde{r}_{\text{leo},l}^{(\text{R,B})}$ is maximized when the SV's ground track is collinear with the baseline. In such cases, using (20), the magnitude of $\tilde{r}_{\text{leo},l}^{(\text{R,B})}$ may be bounded according to

$$\left|\tilde{r}_{\text{leo},l}^{(\text{R,B})}\right| \le \left|g\left(\theta_l^{(\text{B})}, \alpha_l\right)\right|\frac{\Delta r_b\cdot e_{\text{leo},L}}{R_E} \tag{26}$$

where

$$g(\theta,\alpha) = \frac{\frac{1}{\alpha}}{\frac{1}{\sin\theta}-\frac{1}{\sqrt{\alpha^2-\cos^2\theta}}}. \tag{27}$$

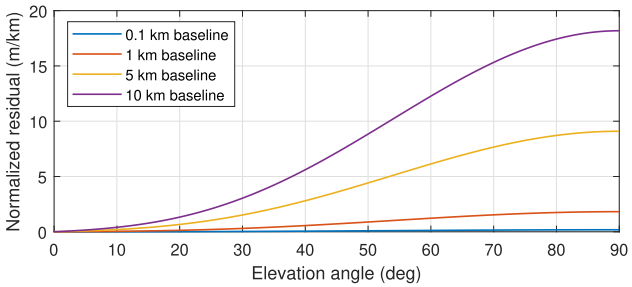

Fig. 4. Normalized residual as a function of the elevation angle for different baseline values.

Fig. 4 shows $|g(\theta_l^{(\mathrm{B})}, \alpha_l)|\frac{\Delta r_b}{R_E}$ as a function of $\theta_l^{(\mathrm{B})}$ for different values of Δr_b. This quantity, called normalized residual, represents the maximum residual error per unit of SV position error.

C. Measurement Errors Due to Atmospheric Effects

In case the LEO receiver is not making corrections for ionospheric and tropospheric delays, a residual error in the CD-LEO measurements will be introduced. In GPS, differential measurements at a "short" baseline of 20 km or less may almost completely cancel out the measurement errors due to atmospheric effects. However, such baselines may still yield significant errors in the CD-LEO measurements. In general, ionospheric and tropospheric delays can be modeled as the product of the delay at zenith and a mapping function of the elevation angle [75], known as the obliquity factor. As the elevation angle of the SV decreases, the obliquity factor increases due to the fact that signals at low elevation angles propagate longer in the ionosphere and troposphere. Differential GNSS exploits the fact that MEO SVs have almost the same elevation angles for a baseline of tens of kilometers, which means that the ionospheric and tropospheric delays cancel out almost completely when forming the differential GNSS measurements. However, LEO SVs are much closer to Earth than MEO SVs, more than 36 times closer in the case of Starlink, which means that the equal elevation angle approximation for typical GNSS baselines does not hold anymore. The residual errors due to atmospheric effects are subsequently studied as a function of the elevation angle and the baseline for LEO SVs.

The ionospheric and tropospheric delays in the carrier phase measurement from the lth LEO SV in the ith receiver can be estimated as

$$\hat{\delta}t_{\mathrm{iono},l}^{(i)} = {}^{\mathrm{z}}\hat{\delta}t_{\mathrm{iono}}^{(i)} f_{\mathrm{iono}}\left(\theta_l^{(i)}\right) \tag{28}$$

$$\hat{\delta}t_{\mathrm{trop},l}^{(i)} = {}^{\mathrm{z,w}}\hat{\delta}t_{\mathrm{trop}}^{(i)} f_{\mathrm{trop,w}}\left(\theta_l^{(i)}\right) + {}^{\mathrm{z,d}}\hat{\delta}t_{\mathrm{trop}}^{(i)} f_{\mathrm{trop,d}}\left(\theta_l^{(i)}\right) \tag{29}$$

where ${}^{\mathrm{z}}\hat{\delta}t_{\mathrm{iono}}^{(i)}$, ${}^{\mathrm{z,w}}\hat{\delta}t_{\mathrm{trop}}^{(i)}$, and ${}^{\mathrm{z,d}}\hat{\delta}t_{\mathrm{trop}}^{(i)}$ are the ionospheric, tropospheric wet, and tropospheric dry delays for the ith receiver at zenith, respectively, and $f_{\mathrm{iono}}(\theta_l^{(i)})$, $f_{\mathrm{trop,w}}(\theta_l^{(i)})$, and $f_{\mathrm{trop,d}}(\theta_l^{(i)})$ are the ionospheric, tropospheric wet, and tropospheric dry obliquity factors, respectively.

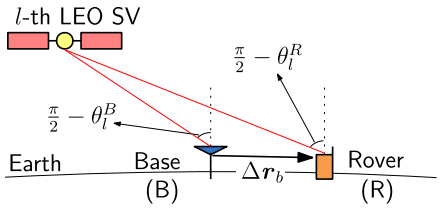

Fig. 5. Base-rover-LEO SV geometry when $\Delta\theta_l$ is maximized, i.e., the 2–D position of the LEO SV is collinear with the base and rover positions.

Assuming that ${}^{\mathrm{z}}\hat{\delta}t_{\mathrm{iono}}^{(\mathrm{R})} = {}^{\mathrm{z}}\hat{\delta}t_{\mathrm{iono}}^{(\mathrm{B})}$ and using a first-order Taylor series expansion of $f_{\mathrm{iono}}(\theta_l^{(\mathrm{R})})$ around $\theta_l^{(\mathrm{B})}$, the residual in the single difference CD-LEO measurement due to ionospheric delays can be approximated as

$$\begin{aligned}\hat{\delta}t_{\mathrm{iono},l}^{(\mathrm{R,B})} &\triangleq \hat{\delta}t_{\mathrm{iono},l}^{(\mathrm{R})} - \hat{\delta}t_{\mathrm{iono},l}^{(\mathrm{B})} \\ &\approx {}^{\mathrm{z}}\hat{\delta}t_{\mathrm{iono}}^{(\mathrm{B})} \cdot \frac{d}{d\theta} f_{\mathrm{iono}}(\theta)\Big|_{\theta_l^{(\mathrm{B})}} \Delta\theta_l \end{aligned} \tag{30}$$

where $\Delta\theta_l \triangleq \theta_l^{(\mathrm{R})} - \theta_l^{(\mathrm{B})}$. Fig. 5 illustrates the geometry between the LEO SV and the base and rover receivers when the 2-D position of the LEO SV is collinear with the base and rover positions. It can be shown that $|\Delta\theta_l|$ is maximized in such configurations. Using the law of sines and assuming that $d_l^{(\mathrm{R})} = d_l^{(\mathrm{B})}$, one can show that

$$|\Delta\theta_l| \le |\Delta\theta_l|_{\max} \tag{31}$$

where $|\Delta\theta_l|_{\max}$ is a function of the baseline and elevation angle at the base receiver given by

$$|\Delta\theta_l|_{\max} \triangleq \left|\sin^{-1}\left[\frac{\sin\theta_l^{(\mathrm{B})}\Delta r_b}{R_E\left(\sqrt{\alpha^2 - \cos^2\theta_l^{(\mathrm{B})}} - \sin\theta_l^{(\mathrm{B})}\right)}\right]\right|. \tag{32}$$

Combining (30) and (31) yields the following bound:

$$\left|\hat{\delta}t_{\mathrm{iono},l}^{(\mathrm{R,B})}\right| \le \left|{}^{\mathrm{z}}\hat{\delta}t_{\mathrm{iono}}^{(\mathrm{B})} \cdot \frac{d}{d\theta} f_{\mathrm{iono}}(\theta)\Big|_{\theta_l^{(\mathrm{B})}}\right| \cdot |\Delta\theta_l|_{\max}. \tag{33}$$

A similar bound is obtained for residuals due to tropospheric delays as

$$\begin{aligned}\left|\hat{\delta}t_{\mathrm{trop},l}^{(\mathrm{R,B})}\right| \le \Bigg|&{}^{\mathrm{z,w}}\hat{\delta}t_{\mathrm{trop}}^{(\mathrm{B})} \cdot \frac{d}{d\theta} f_{\mathrm{trop,w}}(\theta)\Big|_{\theta_l^{(\mathrm{B})}} \\ &+ {}^{\mathrm{z,d}}\hat{\delta}t_{\mathrm{trop}}^{(\mathrm{B})} \cdot \frac{d}{d\theta} f_{\mathrm{trop,d}}(\theta)\Big|_{\theta_l^{(\mathrm{B})}}\Bigg| \cdot |\Delta\theta_l|_{\max}. \end{aligned} \tag{34}$$

Equations (33) and (34) indicate that the magnitude of ionospheric and tropospheric delay residuals will be upper bounded by terms proportional to $|\Delta\theta_l|_{\max}$, which is the maximum difference between the elevation angles of the lth SV with respect to the base and rover, respectively. Fig. 6 shows $|\Delta\theta_l|_{\max}$ as a function of $\theta_l^{(\mathrm{B})}$ for different baseline values. As expected from (32), $|\Delta\theta_l|_{\max}$ is maximized when the SV is at zenith. Moreover, Fig. 6 suggests that the small angle approximation holds with respect to the baseline

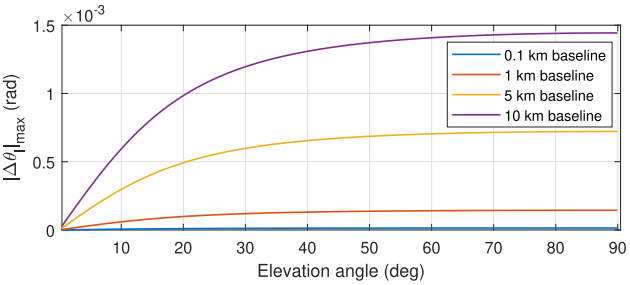

Fig. 6. Plot of $|\Delta\theta_l|_{\max}$ as a function of $\theta_l^{(\mathrm{B})}$ for different baseline values.

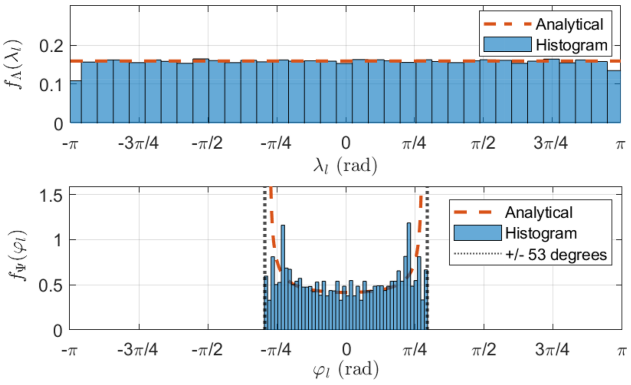

Fig. 7. Histogram and analytical pdfs of λ_l and φ_l for $i = 53^\circ$.

Δr_b. As such, one can approximate the upper bound on the magnitude of the ionospheric and tropospheric delay residuals to be proportional to the baseline.

IV. JOINT DISTRIBUTION OF MEGACONSTELLATION LEO SVS' AZIMUTH AND ELEVATION ANGLES

The joint pdf of megaconstellation LEO SVs' azimuth and elevation angles offers an efficient way to characterize the performance of the CD-LEO framework as well as to enable performance-driven design of the CD-LEO framework, such as the differential baseline selection. To this end, the LEO SV orbits are defined, such as in Section III-A. Moreover, it as assumed that the probability p_j of the lth LEO SV belonging to constellation j is given by

$$p_j \triangleq \Pr\left[\mathrm{SV}_l \in \mathrm{const}_j\right] = \frac{L_j}{L}, \quad j = 1, \ldots, J, l = 1, \ldots, L. \tag{35}$$

The following analysis holds for both receivers; hence, the superscripts j, B, and R will be dropped for simplicity of notation.

A. Satellite Elevation and Azimuth Distribution Model

Let λ_l and φ_l denote the lth LEO SV's longitude and latitude, respectively. Recall that the Earth is assumed to be spherical and the SV orbits are assumed to be circular. Moreover, it is assumed that the right ascension of the ascending node (RAAN) is uniformly distributed over 2π. As such, it can be shown that the pdfs of λ_l and φ_l are given by [63]

$$f_\Lambda(\lambda_l) = \begin{cases} \frac{1}{2\pi}, & 0 \le \lambda_l < 2\pi \\ 0, & \text{elsewhere} \end{cases} \tag{36}$$

$$f_\Psi(\varphi_l) = \begin{cases} \frac{\cos\varphi_l}{\pi\sqrt{\sin^2 i - \sin^2\varphi_l}}, & |\varphi_l| < i \\ 0, & \text{elsewhere} \end{cases} \tag{37}$$

with the joint pdf given by

$$f_{\Lambda,\Psi}(\lambda_l, \varphi_l) = f_\Lambda(\lambda_l) f_\Psi(\varphi_l). \tag{38}$$

The histogram obtained from the Starlink constellation and the analytical pdfs for $i = 53^\circ$ are shown in Fig. 7.

The joint pdf of ϕ_l and θ_l for an SV in constellation j, parameterized by the receiver's longitude λ_0 and latitude φ_0, the normalized orbital radius α_j, inclination angle i_j, and elevation mask $\theta_{\min}$, was derived in [63] and is denoted by ${}^l f_{\Phi,\Theta}^{\theta_{\min}}(\phi_l, \theta_l; \alpha_j, i_j, \lambda_0, \varphi_0)$. This pdf can be obtained from $f_{\Lambda,\Psi}(\lambda_l, \varphi_l)$ through coordinate transformation. To this end, the mapping from the pair (ϕ_l, θ_l) to (λ_l, φ_l) must be established. The result is captured in the following lemma. Note that the subscript j will be omitted for simplicity of notation.

LEMMA IV.1 Given a spherical Earth, an SV orbit characterized by i_l and α_l, and a receiver's longitude λ_0 and latitude φ_0, the inverse mapping from (ϕ_l, θ_l) to (λ_l, φ_l) is given by

$$\boldsymbol{y}(\phi_l, \theta_l) \triangleq \begin{bmatrix} \lambda_l \\ \varphi_l \end{bmatrix} = \begin{bmatrix} \tan^{-1}\left[\frac{a_{02}(\phi_l,\theta_l)}{a_{01}(\phi_l,\theta_l)}\right] \\ \sin^{-1}\left[a_{03}(\phi_l, \theta_l)\right] \end{bmatrix} \tag{39}$$

where

$$\begin{aligned}
a_{01}(\phi_l, \theta_l) &\triangleq \sin\left[\gamma(\theta_l)\right] f_{01}(\phi_l, \theta_l) + \frac{1}{\alpha}\cos\varphi_0\cos\lambda_0 \\
a_{02}(\phi_l, \theta_l) &\triangleq \sin\left[\gamma(\theta_l)\right] f_{02}(\phi_l, \theta_l) + \frac{1}{\alpha}\cos\varphi_0\sin\lambda_0 \\
a_{03}(\phi_l, \theta_l) &\triangleq \sin\left[\gamma(\theta_l)\right] f_{03}(\phi_l, \theta_l) + \frac{1}{\alpha}\sin\varphi_0, \\
f_{01}(\phi, \theta) &\triangleq \cos\varphi_0\cos\lambda_0\tan\theta - \sin\lambda_0\sin\phi \\
&\quad - \sin\varphi_0\cos\lambda_0\cos\phi \\
f_{02}(\phi, \theta) &\triangleq \cos\varphi_0\sin\lambda_0\tan\theta + \cos\lambda_0\sin\phi \\
&\quad - \sin\varphi_0\sin\lambda_0\cos\phi \\
f_{03}(\phi, \theta) &\triangleq \sin\varphi_0\tan\theta + \cos\varphi_0\cos\phi.
\end{aligned}$$

PROOF See Appendix A. ■

Finally, $f_{\Phi,\Theta}(\phi_l, \theta_l)$ is given by

$$f_{\Phi,\Theta}(\phi_l, \theta_l) = \begin{cases} \frac{|\det[\mathbf{J}_y(\phi_l,\theta_l)]|\sqrt{1-a_{03}^2(\phi_l,\theta_l)}}{2\pi^2\sqrt{\sin^2 i - a_{03}^2(\phi_l,\theta_l)}}, & |a_{03}(\phi_l, \theta_l)| < \sin i \\ 0, & \text{elsewhere} \end{cases} \tag{40}$$

where $\mathbf{J}_y(\phi_l, \theta_l) \triangleq \begin{bmatrix} \frac{\partial\lambda_l}{\partial\phi_l} & \frac{\partial\lambda_l}{\partial\theta_l} \\ \frac{\partial\varphi_l}{\partial\phi_l} & \frac{\partial\varphi_l}{\partial\theta_l} \end{bmatrix}$. The expression of $\mathbf{J}_y(\phi_l, \theta_l)$ and its determinant are given in Appendix B.

B. Azimuth and Elevation Joint Distribution for a Set Elevation Mask

Since the visible SVs have nonnegative elevation angles, one is interested to know the pdf for $\theta_l \ge 0$. In practice, a

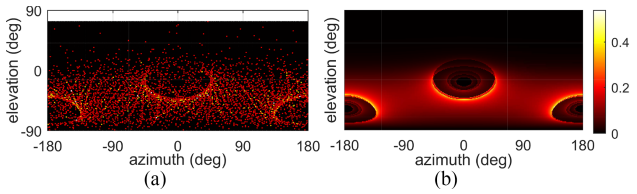

Fig. 8. Joint (ϕ_l, θ_l) pdfs calculated from (a) a histogram of azimuth and elevation angles of the SVs from the proposed Starlink LEO constellation and (b) from the analytical solution in (43). Note that the different orbital shells can be seen in the pdfs, especially in the analytical one in (b). The receiver is located at $\varphi_0 = 33.642673^\circ$, $\lambda_0 = -117.838747^\circ$, and zero altitude. .

positive elevation mask $\theta_{\min}$ is set. The pdf for $\theta_l \geq \theta_{\min}$ is hence given by

$$f^{\theta_{\min}}_{\Phi,\Theta}(\phi_l, \theta_l) = \begin{cases} \frac{|\det[\mathbf{J}_y(\phi_l,\theta_l)]|\sqrt{1-a_{03}^2(\phi_l,\theta_l)}}{C_{l,\theta_{\min}}\sqrt{\sin^2 i - a_{03}^2(\phi_l,\theta_l)}}, & (\phi_l, \theta_l) \in \mathcal{D}_{l,\theta_{\min}} \\ 0, & \text{elsewhere} \end{cases} \quad (41)$$

where the domain $\mathcal{D}_{l,\theta_{\min}}$ is defined as

$$\mathcal{D}_{l,\theta_{\min}} = \left[(\phi_l, \theta_l)\,|(|a_{03}(\phi_l, \theta_l)| < \sin i) \cap (\theta_l \geq \theta_{\min})\right]$$

and the normalization constant $C_{l,\theta_{\min}}$ is given by

$$C_{l,\theta_{\min}} = 2\pi^2 \int\int_{\mathcal{D}_{l,\theta_{\min}}} f_{\Phi,\Theta}(\phi_l, \theta_l) d\phi_l d\theta_l.$$

Note that one can find the average number of visible satellites $\bar{L}$ according to

$$\bar{L} = L \times \Pr[\theta_l \geq \theta_{\min}] = L\frac{C_{l,\theta_{\min}}}{2\pi^2} \quad (42)$$

where L is the total number of SVs in the constellation.

C. Multiconstellation Azimuth and Elevation Joint Distribution

Recall that the pdf in (41) is constellation-specific, i.e., it is parameterized by one inclination angle $i = i_j$ and one normalized orbital radius $\alpha = \alpha_j$. For the case of multiconstellations, as is the case for LEO megaconstellation, the joint pdf for all constellations, each of which defined by is given by

$${}^{\text{all}}f^{\theta_{\min}}_{\Phi,\Theta}(\phi_l, \theta_l) = \sum_{j=1}^{J} p_j\, {}^{j}f^{\theta_{\min}}_{\Phi,\Theta}(\phi_l, \theta_l) \quad (43)$$

where ${}^{j}f^{\theta_{\min}}_{\Phi,\Theta}(\phi_l, \theta_l)$ is the pdf of the jth constellation obtained according to (41). Fig. 8 shows the joint pdf of (ϕ_l, θ_l) estimated from a histogram of azimuth and elevation angles of the proposed Starlink constellation as well as the analytical pdf calculated in (43). The receiver location was set in Irvine, CA, USA, with $\varphi_0 = 33.642673^\circ$, $\lambda_0 = -117.838747^\circ$, zero altitude. It can be seen that the two pdfs match closely.

V. PERFORMANCE CHARACTERIZATION AND PERFORMANCE-DRIVEN CD-LEO FRAMEWORK DESIGN

This section studies leverages the models developed in Section III and Section IV to develop a performance characterization methodology that can inform the design of CD-LEO frameworks, namely, in baseline selection. First, the cdf and statistics of the PDOP are evaluated, followed by the statistics and cdfs of the CD-LEO measurement residual errors due to ephemeris errors and atmospheric effects. Note that the following analysis is concerned with the single-epoch position estimation performance after the integer ambiguities have been resolved, i.e., for the PS-WNLS. The performance characterization is conducted using a Monte Carlo approach: several realizations of the elevation and azimuth angles are obtained from the joint pdf derived in Section IV and the cdf or statistics of the performance metric are computed numerically. To do so, the average number of visible satellites $\bar{L}$ is determined according to (42) and the elevation mask. Then, $\bar{L}$ realizations of joint azimuth and elevation angles are determined by sampling the joint PDF given in (43). The PDF is sampled using a standard rejection sampling method [79]. Then, the variable of interest is calculated as a function of the azimuth and elevation angle in realization. Finally, the cdf of the variable of interest is computed from all the Monte Carlo realizations. It is important to note that the same methodology can be used to characterize performance in different environments, such as multipath errors or SV visibility in deep urban canyons.

A. PDOP Statistics Characterization

One important measure of the estimability (i.e., degree of observability) of the receiver's position is the PDOP. Assuming equal measurement noise variances, the PDOP in the CD-LEO framework is given by $\text{PDOP} = \sqrt{\text{trace}[\mathbf{P}]}$, where $\mathbf{P}$ is the PDOP matrix given by

$$\mathbf{P} = 2\left[\mathbf{G}^{\mathrm{T}}\mathbf{T}^{\mathrm{T}}\left(\mathbf{T}\mathbf{T}^{\mathrm{T}}\right)^{-1}\mathbf{T}\mathbf{G}\right]^{-1}. \quad (44)$$

Another metric of interest is the horizontal dilution of precision (HDOP), which gives a measure of the estimability of the horizontal components of the position vector. This metric is appropriate to study in the case where the rover is equipped with an altimeter and is using LEO signals mainly to estimate its horizontal position. Otherwise, the vertical dilution of precision (VDOP) becomes an important metric to study as well. The HDOP is calculated according to $\text{HDOP} = \sqrt{\text{trace}[\mathbf{P}_{2\times2}]}$, where $\mathbf{P}_{2\times2}$ indicates the 2×2 block of the PDOP matrix corresponding to the horizontal position coordinates, and the VDOP is given by $\text{VDOP} = \sqrt{\mathbf{P}_{3\times3}}$, where $\mathbf{P}_{3\times3}$ is the third diagonal element of $\mathbf{P}$, corresponding to the vertical position coordinate. The PDOP, HDOP, and VDOP cdfs are characterized numerically using the pdfs of the SV azimuth and elevation angles derived in Section IV for the Starlink constellation with the parameters in Table I. The cdfs, shown in Fig. 9 are computed for a receiver in Irvine, CA, USA, with

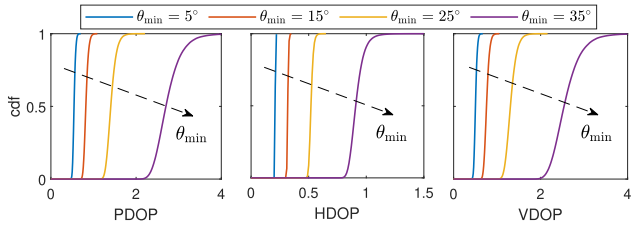

Fig. 9. Cdf of the PDOP, HDOP, and VDOP in the CD-LEO framework for the Starlink constellation for a receiver located at $\varphi_0 = 33.642673°$, $\lambda_0 = -117.838747°$, and zero altitude. The dashed arrows indicate the direction of the curves when $\theta_{\min}$ increases. The cdfs were computed from 10^5 PDOP, HDOP, and VDOP realizations.

$\varphi_0 = 33.642673°$, $\lambda_0 = -117.838747°$, zero altitude, and for four elevation angle masks: 5°, 15°, 25°, and 35°. While 5° might be unrealistically low for LEO SVs, it is included in the analysis to study a wider range of the DOP values. Fig. 9 shows that the PDOP is mostly less than 2 for elevation angle masks of 25° or below, and above 2 almost all the time for elevation angle masks of 35°. This is mainly due to the fact that the vertical component becomes poorly observable for such elevation angle masks. This is validated in the HDOP cdf, which shows that the HDOP is almost always below unity for elevation masks of 35° or below. In fact, the HDOP is mostly below 0.6 for elevation angles of 25°, showing that highly accurate horizontal positioning may be achieved.

Moreover, heat maps showing the average PDOP, HDOP, and VDOP were computed in Fig. 10. The figure shows that the average DOP is less than 1.5 for all latitudes between $-60°$ and 60°. Note that only the aforementioned range of latitudes is considered as 1) this is the region of interest and 2) the elevation angles become very low and the SVs are obstructed at the poles as the orbits have a 55 ° inclination yielding very large DOP values.

B. Measurement Error Statistics Characterization

1) *Ephemeris Errors:* The cdf of $|\tilde{r}_{\text{leo}_l}^{(\text{R,B})}|$ can be characterized from (26) and the joint distribution of the LEO SVs' azimuth and elevation angles derived in Section IV. To this end, the cdf of $g(\theta, \alpha)$ is calculated for the Starlink LEO constellation using the parameters in Table I. The receiver was assumed to be on the University of California, Irvine (UCI) campus. The cdf was computed for three elevation masks: $\theta_{\min} = 5°$, $\theta_{\min} = 25°$, and $\theta_{\min} = 35°$. The cdf of $g(\theta, \alpha)$ is shown in Fig. 11(a), and the expected value of $g(\theta, \alpha)$, denoted by $\mathbb{E}[g(\theta, \alpha)]$, is shown in Fig. 11(b) as a function of $\theta_{\min}$.

Next, to characterize the effect of ephemeris errors on CD-LEO measurements, the measurement errors are computed for a given distribution of the SV position error. The distribution of the SV position error was obtained from published root mean-squared error (RMSE) data by Celestrack for current Starlink SVs, which represent the SV position RMSE at the TLE epoch. A histogram of the SV position RMSE as well as a pdf fit are shown in Fig. 12. It was found that the Burr distribution best fit the RMSE data. It is assumed that the SV position error is independent

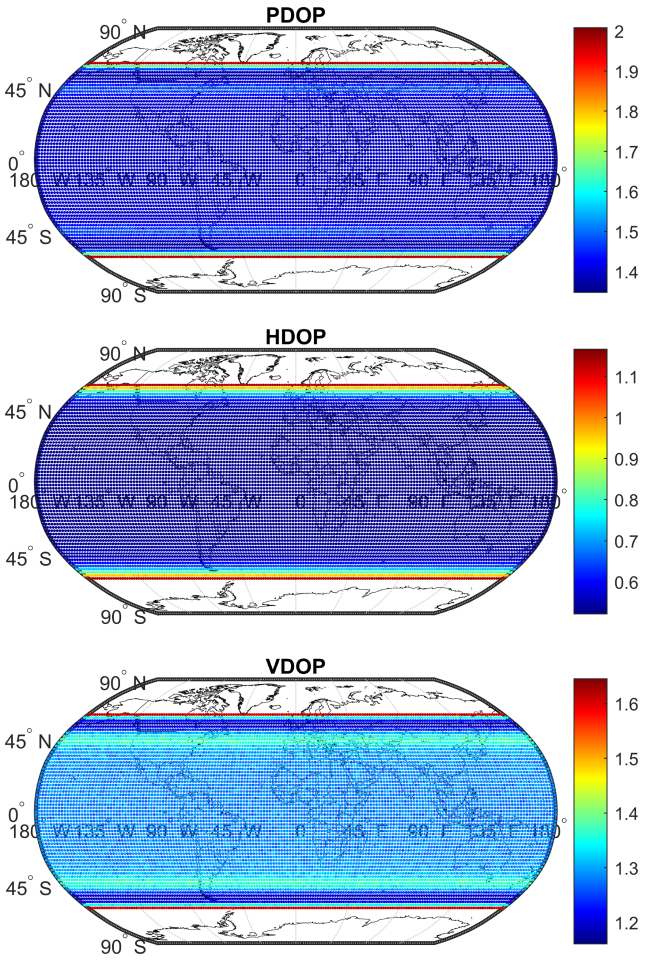

Fig. 10. Heat maps of the average PDOP, HDOP, and VDOP for the CD-LEO navigation framework. The heat maps were computed from 10^3 PDOP, HDOP, and VDOP realizations for an elevation mask of 25°.

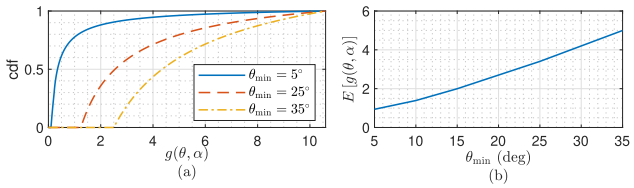

Fig. 11. (a) Cdf of $g(\theta, \alpha)$ for $\theta_{\min} = 5°$, $\theta_{\min} = 25°$, and $\theta_{\min} = 35°$. (b) Expected value of $g(\theta, \alpha)$ as a function of $\theta_{\min}$.

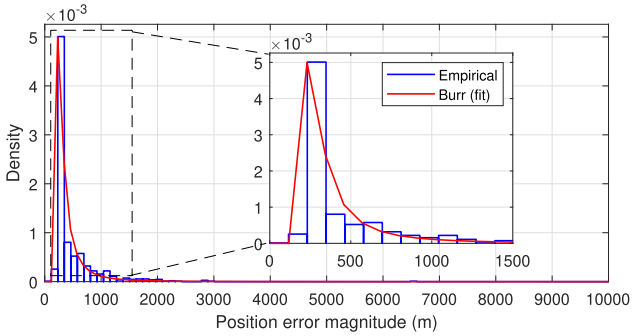

Fig. 12. Histogram of Starlink LEO SV position RMSE as obtained from Celestrack along with a pdf fit. It was found that the Burr distribution best fit the empirical data.

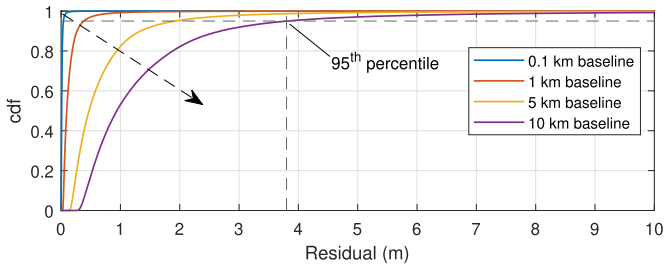

Fig. 13. Cdf of the CD-LEO measurement error due to SV position errors. The dashed arrows indicate the direction of the curves when the baseline increases. The cdf was computed from 10^5 residual realizations.

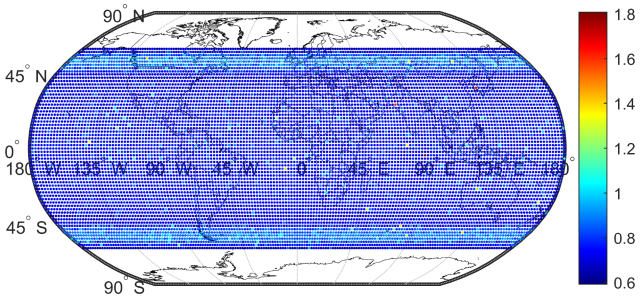

Fig. 14. Heat map of the average measurement error magnitude in CD-LEO measurements due to SV position error for a 5-km baseline. The heat map was computed from 10^4 residual realizations.

of the SV azimuth and elevation angles; hence, it is sampled independently from the Burr distribution fit.

Fig. 13 shows the cdf of the measurement errors for $\theta_{\min} = 25^\circ$ and for different values of the baseline. The SV position errors were drawn from the Burr distribution described above. The receiver was assumed to be on the UCI campus. The black arrow indicates the direction in which the baseline increases. It can be seen from Fig. 13 that the 95th percentile for a 10-km baseline is 3.8 m, which indicates that the measurement error 95th percentile is lower than 3.8 m for all baselines less than 10 km.

A heat map of the average measurement error magnitude is then computed for a baseline of 5 km and shown in Fig. 14. The heat map shows that the average measurement error in the CD-LEO measurements due to SV position error is less than 2 m almost anywhere between -60° and 60° latitudes.

2) *Atmospheric Effects:* Since the ${}^{\mathrm{z}}\hat{\delta}t^{(i)}_{\mathrm{iono},l}$, ${}^{\mathrm{z,w}}\hat{\delta}t^{(i)}_{\mathrm{iono},l}$, and ${}^{\mathrm{z,d}}\hat{\delta}t^{(i)}_{\mathrm{trop},l}$ are also functions of several unknown parameters, such as carrier frequency, TECV, atmospheric pressure, temperature, etc., the effect of ionospheric and tropospheric delays on CD-LEO measurements will be characterized through the mapping functions derived from (33) and (34) as

$$\bar{f}_{\mathrm{iono}}(\theta) \triangleq \left| \frac{d}{d\theta} f_{\mathrm{iono}}(\theta) \Delta\theta_{\max} \right| \tag{45}$$

$$\bar{f}_{\mathrm{trop,w}}(\theta) \triangleq \left| \frac{d}{d\theta} f_{\mathrm{trop,w}}(\theta) \Delta\theta_{\max} \right| \tag{46}$$

$$\bar{f}_{\mathrm{trop,d}}(\theta) \triangleq \left| \frac{d}{d\theta} f_{\mathrm{trop,d}}(\theta) \Delta\theta_{\max} \right|. \tag{47}$$

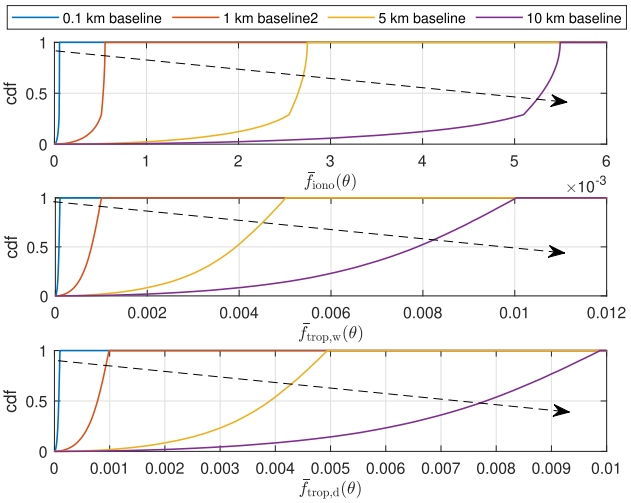

Fig. 15. Cdf of the ionospheric and tropospheric delay mapping functions in (45)–(47) for $\theta_{\min} = 25^\circ$. The dashed arrows indicate the direction of the curves when the baseline increases. The cdf was computed from 10^5 realizations.

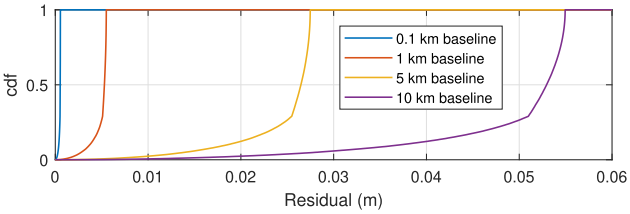

Fig. 16. Cdf of the error in the CD-LEO measurements due to the ionospheric delays for $\theta_{\min} = 25^\circ$ and ionospheric delay of 10 m at zenith. The cdf was computed from 10^5 residual realizations.

The cdf of $\bar{f}_{\mathrm{iono}}(\theta)$, $\bar{f}_{\mathrm{trop,w}}(\theta)$, and $\bar{f}_{\mathrm{trop,d}}(\theta)$ are shown in Fig. 15. The cdf of the measurement errors can be computed knowing the ionospheric and wet and dry tropospheric delays by simply multiplying them by the corresponding mapping functions in (45)–(47). For example, Fig. 16 shows the cdf of the CD-LEO measurement error due to ionospheric delays for an ionospheric delay of 10 m at zenith.

Heat maps of the average ionospheric and tropospheric delay mapping functions are then computed for a baseline of 5 km and shown in Fig. 17. The heat maps show that the average error magnitude in the CD-LEO measurements due to ionospheric delays is less than 4 mm per meters of zenith ionospheric delay almost anywhere between -60° and 60° latitudes.

REMARK 2 It is important to note that the goal of the article is to develop a methodology for characterizing the performance of a CD-LEO system and designing key system parameters. The Starlink constellation is taken as an example and several values for the baselines were considered for illustrative purposes. Other values of the baseline can be evaluated as well. Designing the CD-LEO baseline is a function of available resources and desired performance. Such a study is beyond the scope of this article and is left as future work.

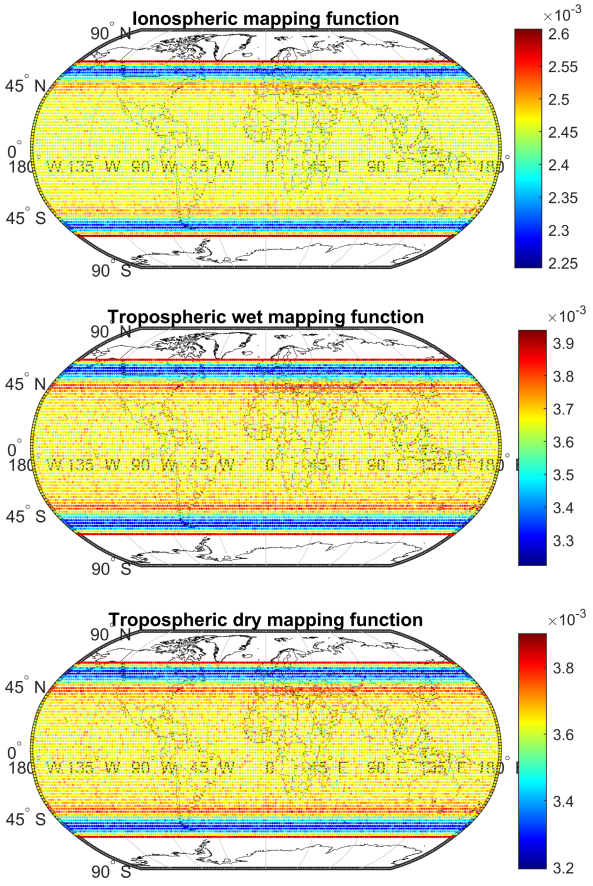

Fig. 17. Heat map of the average ionospheric and tropospheric delay mapping functions for a 5 km baseline. The heat map was computed from 10^4 residual realizations.

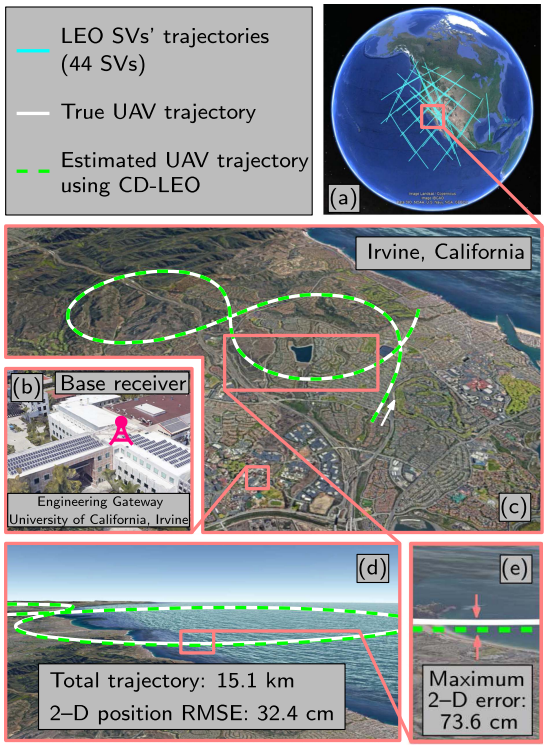

Fig. 18. Simulation results showing a fixed-wing UAV navigating using the proposed CD-LEO framework. (a) Starlink LEO SVs' trajectories (elevation mask set at 15°). (b) Base receiver location. (c) True and estimated UAV trajectories. (d)–(e) Close-up of the UAV trajectory showing precise navigation with the CD-LEO framework and a maximum 2–D position error of 73.6 cm.

VI. SIMULATION RESULTS

This section details simulation results of a fixed-wing UAV navigating with signals from the proposed Starlink LEO SV megaconstellation under the double difference CD-LEO framework discussed in Section II. The UAV, representing the rover, flew a total trajectory of 15.1 km in 300 s over Irvine, CA. The simulated UAV compares in performance to a small private plane with a cruise speed of roughly 50 m/s. The trajectory of the UAV, shown in white in Fig. 18(c) consisted of a straight segment, followed by a figure-eight pattern over Irvine, CA, USA, and then a final straight segment. The UAV flew at a constant altitude of 2.5 km, while executing the rolling and yawing maneuvers. A stationary base, shown in Fig. 18(b), was located on top of the Engineering Gateway at the UCI campus. The distance between the base and the UAV throughout the UAV's trajectory ranged between a maximum of 3.826 km to a minimum of 2.489 km. The elevation angle mask was set to 15° in both receivers. The UAV and base station both received signals from 44 simulated LEO SVs, whose trajectories are depicted in blue in Fig. 18(a). To simulate ephemeris errors, the true anomaly of each satellite was randomly shifted such that the satellite position errors were distributed between 75 m and 3.5 km. It was assumed that the UAV had access to GNSS for the first 50 s, during which the B-WNLS is solved. After 50 s, the UAV solves for its 3-D position using CD-LEO measurements and the integer ambiguities estimates obtained by solving the B-WNLS. The total 3-D and 2-D position RMSE were 2.2 m and 32.4 cm, respectively, while the maximum 2-D position error was 73.6 cm. Given that the baseline ranges from 2.5 to 3.8 km, the cdf of the measurement errors will be between the red and yellow curves in Fig. 9. As such, measurement errors on the order of 1 m are expected due to ephemeris errors. Note that the signal wavelength was assumed to be 3 cm (10 GHz). Therefore, the ephemeris errors will dominate the measurement errors. Moreover, similar to GNSS, the vertical uncertainty in the CD-LEO framework is larger than the horizontal uncertainty due to less geometric diversity in the vertical direction since the VDOP will be high relative to the HDOP, as seen in Figs. 9 and 10. The simulation layout and the true and estimated UAV trajectories are shown in Fig. 18.

VII. EXPERIMENTAL RESULTS

This section presents experimental results of a UAV navigating with signals from Orbcomm LEO SVs via the CD-LEO framework discussed in Section II. First, the experimental setup is discussed. Then, the navigation frameworks implemented in the experiments and their associated results are presented.

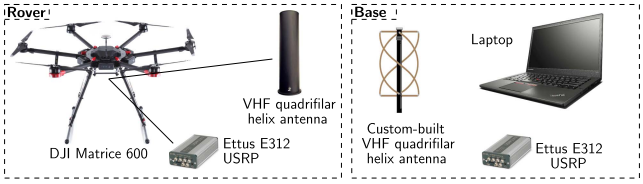

Fig. 19. Base/rover experimental setup of the CD-LEO framework.

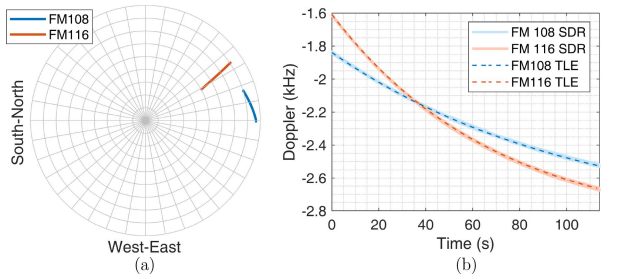

Fig. 20. (a) Sky plot of the geometry of the 2 Orbcomm SVs during the experiment. (b) The measured Doppler frequencies using the proprietary SDR and the expected Doppler calculated from the TLE for both Orbcomm SVs.

A. Experimental Setup

To demonstrate the CD-LEO framework discussed in Section II, the rover was a DJI Matrice 600 UAV equipped with an Ettus E312 USRP, a high-end VHF antenna, and a small consumer-grade GPS antenna to discipline the on-board oscillator. The base was a stationary receiver equipped with an Ettus E312 USRP, a custom-made VHF antenna, and a small consumer-grade GPS antenna to discipline the on-board oscillator. The receivers were tuned to a 137-MHz carrier frequency with 2.4-MHz sampling bandwidth, which covers the 137–138-MHz band allocated to Orbcomm SVs. Samples of the received signals were stored for off-line postprocessing using the software-defined radio (SDR) developed in [21]. The LEO carrier phase measurements were produced at a rate of 4.8 kHz and were downsampled to 10 Hz. The the base's position was surveyed on Google Earth, and the UAV trajectory was taken from its on-board navigation system, which uses GNSS (GPS and GLONASS), an inertial measurement unit (IMU), and other sensors. The hovering horizontal precision of the UAV is reported to be 1.5 m by DJI. The experimental setup is shown in Fig. 19. The UAV traversed a total trajectory of 2.28 km in 120 s.

Over the course of the experiment, the receivers onboard the base and the UAV were listening to two Orbcomm SVs, namely, FM 108 and FM 116. The SVs transmit a telemetry message which includes system time, SV position, and SV velocity as estimated by their on-board GPS receivers. These positions were decoded and used as ground-truth. A position estimate of FM 108 and FM 116 was also obtained from TLE files and SGP4 software [80]. The satellites were simultaneously visible for 2 min. A sky plot of the 2 Orbcomm SVs is shown in Fig. 20(a). The Doppler frequency measured by the rover using the SDR in [21] for the 2 Orbcomm SVs is shown along

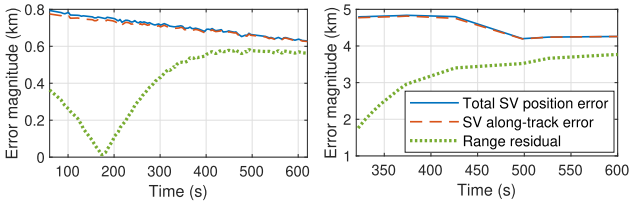

Fig. 21. Total SV position error magnitude and along-track SV position error magnitude for 2 Orbcomm LEO SVs, as well as the range residual due to ephemeris errors as observed by a terrestrial LEO receiver. .

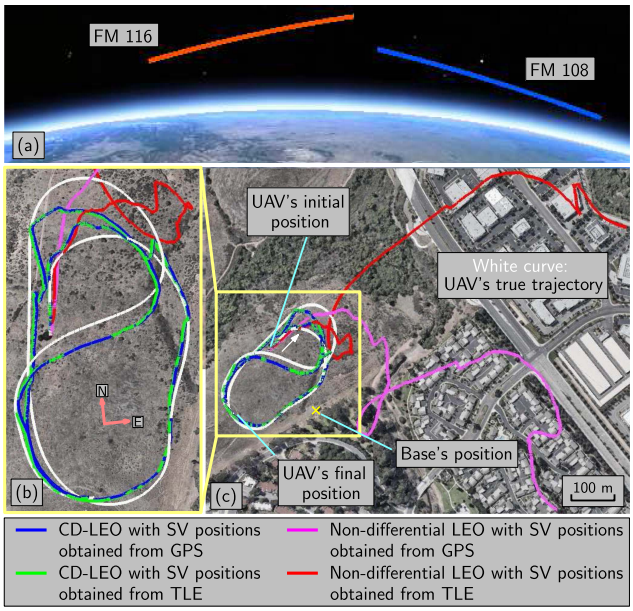

Fig. 22. (a) Trajectories of the 2 Orbcomm LEO SVs. (b)–(c) True and estimated trajectories of the UAV. Map data: Google Earth.

the expected Doppler calculated from the TLE files in Fig. 20(b). The SV position error and the range residuals are shown in Fig. 21 for each SV. Fig. 22(a) shows the SV trajectories. Note that the base and rover were closer than 1 km over the experiment; hence, ionospheric and tropospheric delay residuals were negligible. Since only two satellites were visible at a time, which is typically the case the Orbcomm constellation [53], the single difference CD-LEO framework discussed in Section II is used to estimate the 3–D position and velocity of the UAV from single difference CD-LEO measurements along with altitude measurements, taken from the UAV's on-board navigation solution. To demonstrate the potential of the CD-LEO navigation framework, two frameworks were implemented for comparison: 1) the CD-LEO framework discussed in Section II-D and 2) a nondifferential framework that employs carrier phase LEO measurements from the UAV's receiver only. The second framework is exactly equivalent to the one proposed [81] except that carrier phase measurements from LEO satellites are used instead of cellular transmitters. The results of each framework are presented next.

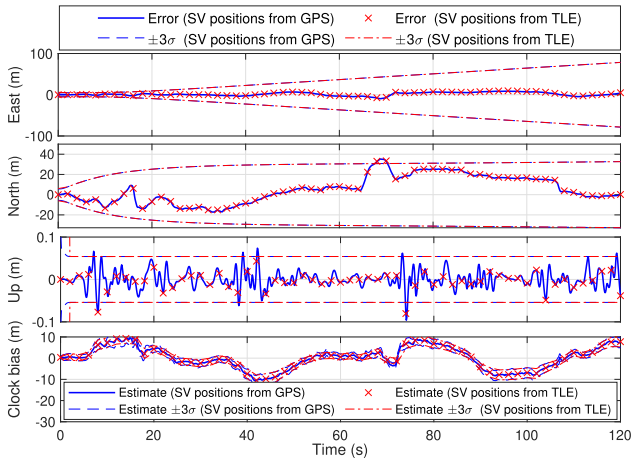

Fig. 23. EKF position estimation error and $\pm 3\sigma$ bounds for the CD-LEO framework. The estimates and sigma bounds for the case where SV positions are obtained from GPS and the ones for the case where the SV positions are obtained from TLE files are almost identical. The top legend corresponds to the position errors and the bottom legend corresponds to the clock bias estimate.

B. CD-LEO Framework Experimental Results

Single difference measurements provide more information on the SV-to-receiver geometry than double difference measurements since the differencing matrix $\mathbf{T}$ is not applied [82]. This comes at the cost of an additional state to be estimated: the common clock bias $\delta t_r^{(\mathrm{R,B})}(k)$. To this end, the UAV's position and velocity states were estimated along with the common clock bias $\delta t_r^{(\mathrm{R,B})}(k)$ and the constant ambiguity $N_2^{(\mathrm{R,B})}$. Note that $N_1^{(\mathrm{R,B})}$ was lumped into $\delta t_r^{(\mathrm{R,B})}(k)$. The UAV's continuous-time acceleration process noise spectra were set to $\tilde{q}_x = \tilde{q}_y = 1\ \mathrm{m}^2/s^5$ and $\tilde{q}_z = 0.01\ \mathrm{m}^2/s^5$ for the East, North, and up components, respectively. The choice of these spectra follows from the fact that the UAV is maneuvering in the horizontal direction only. The position and velocity process noise covariance can be readily obtained from these power spectra [76]. The UAV's and base's oscillator quality is assumed to be that of a typical temperature-compensated crystal oscillator (TCXO), from which the process noise covariance can also be readily obtained according to [76]. A prior for the UAV position and velocity was obtained from the UAV's on-board system. The prior was used to initialize the EKF. After initialization, the EKF was using single-difference Orbcomm LEO SV measurements to estimate the states of the UAV. To study the effect of ephemeris errors on the navigation solution, two EKFs were implemented: 1) one that uses the Orbcomm LEO SV positions estimated by the SVs' on-board GPS receiver and 2) one that uses the Orbcomm LEO SV positions estimated from TLE files. The estimated trajectories are shown in Fig. 22(b) and (c). The EKF position estimation errors are shown in Fig. 23 along with the 3σ bounds. Note that since the UAV mainly travels in the North direction, the East direction becomes poorly estimable; hence, the 3σ bounds in the East direction increase at a higher rate than the 3σ bound in the North direction, as shown in Fig. 23. The common clock bias estimate and the corresponding $\pm 3\sigma$ bounds are also shown in Fig 23. The 3-D position RMSEs and final errors for both EKFs are shown in Table II.

TABLE II
Experimental Results: 3-D RMSEs and 3-D Final Errors

Framework	SV position source	RMSE	Final error
CD-LEO	GPS	14.8 m	3.9 m
CD-LEO	TLE	15.0 m	4.8 m
Nondifferential	GPS	338.6 m	590.4 m
Nondifferential	TLE	405.4 m	759.5 m

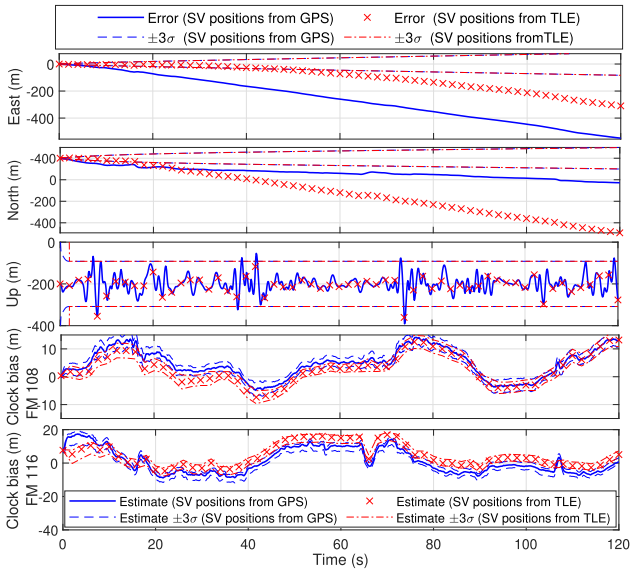

Fig. 24. EKF position estimation error and $\pm 3\sigma$ bounds for nondifferential LEO framework. The sigma bounds for the case where SV positions are obtained from GPS and the ones for the case where the SV positions are obtained from TLE files are almost identical. The top legend corresponds to the position errors and the bottom legend corresponds to the clock bias estimate. Also note that in the nondifferential framework, two clock biases are estimated: one for each SV.

C. Nondifferential LEO Framework Experimental Results

To demonstrate the importance of the CD-LEO framework, a nondifferential LEO framework is implemented. To this end, the UAV's position and velocity are estimated in an EKF using the nondifferential measurements in (1). In this case, two clock biases must be estimated capturing the difference between the receiver's clock bias and each of the Orbcomm LEO SVs' bias. The same dynamics models and initialization method employed in Section VII-B were used in the nondifferential framework, except that the SV's oscillators was assumed to be that of typical oven-controlled crystal oscillators (OCXO) [76]. Similarly to Section VII-B, two EKFs were implemented: 1) one that uses the Orbcomm LEO SV positions estimated by the SVs' on-board GPS receiver and 2) one that uses the Orbcomm LEO SV positions estimated from TLE files. The estimated trajectories are shown in Fig. 22(b) and (c). The EKF position estimation errors are shown in Fig. 24 along with the associated 3σ bounds. The clock bias estimates associated with FM 108

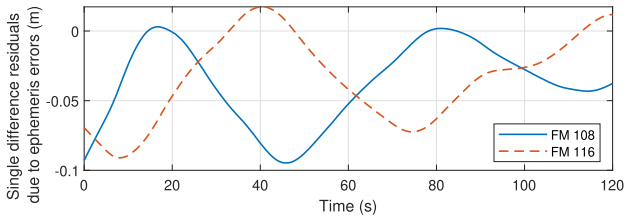

Fig. 25. Single difference residuals due to ephemeris errors for Orbcomm LEO SVs FM 108 and FM 116.

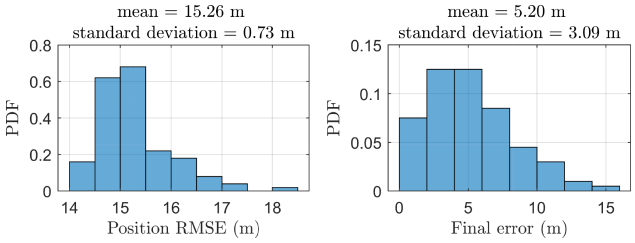

Fig. 26. Histogram of the position RMSE and final error obtained from 100 Monte Carlo realizations, where the initial position estimate of the UAV is drawn from a Gaussian distribution centered at the true UAV position with covariance $9 \times \mathbf{I}_{3\times 3}\text{m}^2$.

and FM 116 and the corresponding $\pm 3\sigma$ bounds are also shown in Fig 24. The 3-D position RMSEs and final errors for both EKFs are shown in Table II.

D. Discussion

Table II summarizes the experimental results for the CD-LEO and nondifferential LEO frameworks. It can be seen from Fig. 21 that the residuals in the nondifferential carrier phase measurements are on the order of kilometers, which explains the unacceptably large RMSEs of the nondifferential framework. While using the SV positions transmitted by the Orbcomm SVs reduces the RMSEs, the errors remain unacceptably large in the nondifferential framework due to other unmodeled errors. Such errors cancel out in the CD-LEO framework, yielding acceptable performance whether SV positions from GPS or TLE are used. The accuracy of these results is *unprecedented*, considering that 1) only 2 LEO SVs were used, 2) no other sensors were fused into the navigation, and 3) these LEO SVs are not intended for navigation and are exploited opportunistically. The predicted single difference residual due to ephemeris errors, $\{\tilde{r}^{\text{R,B}}_{\text{leo},l}\}_{l=1}^{2}$ were calculated according to (19), and are shown in Fig. 25. During the experiment, the baseline varied between 20 and 200 m. According to Section II-A, the function $g(\theta, \alpha)$ averages to 1.346 for the Orbcomm constellation, which has an inclination angle of 45° and orbital altitude of 800 km and $\theta_{\min} = 5°$. From the SV position errors in Fig. 21, the expected range of the residuals is from 0.3 to 16 cm. It can be seen from Fig. 25 that the magnitude of the single difference residual is on the order of *centimeters* and matches the expected values, showing 1) the robustness of the CD-LEO framework against ephemeris errors and 2) the accuracy of the performance analysis framework discussed in Section V. These small residuals explain the small change in performance between using TLE-derived SV positions and GPS-derived SV positions in the differential framework.

REMARK 3 To see the effect of small initialization errors on the CD-LEO framework performance, the EKF for the CD-LEO framework with SV position obtained from TLE was randomized over 100 Monte Carlo realizations. The initial estimate was drawn from a Gaussian distribution centered at the true UAV position with covariance $9 \times \mathbf{I}_{3\times 3}$ m^2. The histograms of the position RMSE and final error are shown in Fig. 26 along with their means and standard deviations. The results show that the EKF is robust against small initial errors.

REMARK 4 The CD-LEO frameworks were also implemented without altimeter measurements. The 3-D position RMSE and final position error when using SV position estimates from GPS were calculated to be 15.1 and 15.0 m, respectively. The 3-D position RMSE and final position error when using SV position estimates from TLE were calculated to be 14.3 and 8.4 m, respectively. Note that the RMSE in the latter case improved slightly; however, the final error degraded significantly. Nevertheless, the performance obtained with only CD-LEO measurements is comparable with that of CD-LEO and altimeter.

REMARK 5 In order to test the double difference framework, the CD-LEO framework was also implemented with the UAV acting as the base and the stationary receiver acting as a stationary rover. The 2-D position error of the stationary rover after the B-WNLS was calculated to be 10.9 m when using SV position estimates from TLE, and 8.2 m when using SV position estimates from GPS. The HDOP was found to be 29.2. Assuming a precision of $\lambda/2$ in the CD-LEO measurements, it is found that the position errors obtained in this experiment are well below the 1σ bound.

VIII. CONCLUSION

This article proposes a differential framework for opportunistic navigation with carrier phase measurements from megaconstellation LEO satellites. Models of the measurement errors due to ephemeris errors and ionospheric and tropospheric delays were derived as a function of the SV elevation angle. Moreover, the joint pdf of the megaconstellation LEO satellites' azimuth and elevation angle was characterized. A performance characterization of the proposed CD-LEO framework was conducted using derived joint azimuth and elevation angle pdf, showing the potential of LEO satellite signals for precise navigation. The performance characterization conducted in this article also facilitates system parameter design to meet desired performance requirements. Simulation and experimental results are presented showing a UAV localizing itself with LEO satellite signals using carrier phase differential measurements to an unprecedented level of accuracy. The simulation results show a UAV navigating for 15.1 km in 300 s, while using

signals from 44 Starlink LEO satellites, achieving a 3-D position RMSE of 2.2 m and a 2-D RMSE of 32.4 cm. The experimental results show a UAV navigating for 2.28 km in 2 min over Aliso Viejo, CA, USA, using exclusively signals from only two Orbcomm LEO satellites, achieving a position RMSE of 14.8 m. Additional experiments could be conducted to characterize the CD-LEO performance with varying baselines in future work.

ACKNOWLEDGMENT

The authors would like to thank Dr. Chris Bartone for the insightful discussions and Joshua Morales, MyLinh Nguyen, Ali Abdallah, Mohammad Orabi, Kimia Shamaei, Mahdi Maaref, and Naji Tarabay for their help in data collection.

APPENDIX A
PROOF OF LEMMA IV.1

This appendix proves the inverse mapping from (ϕ_l, θ_l) to (λ_l, φ_l) is given in Lemma IV.1.

PROOF For a spherical Earth, the lth satellite position in Earth-centered Earth-fixed (ECEF) may be expressed as

$$\bar{\boldsymbol{r}}_{\text{leo},L} = \alpha_l R_E \left[\cos\varphi_l \cos\lambda_l, \quad \cos\varphi_l \sin\lambda_l, \quad \sin\varphi_l\right]^{\mathrm{T}}.$$

Subsequently, given $\bar{\boldsymbol{r}}_{\text{leo},L}$, the longitude and latitude λ_l and φ_l, respectively, may be obtained according to

$$\lambda_l = \tan^{-1}\left[\frac{\boldsymbol{e}_2^{\mathrm{T}}\bar{\boldsymbol{r}}_{\text{leo},L}}{\boldsymbol{e}_1^{\mathrm{T}}\bar{\boldsymbol{r}}_{\text{leo},L}}\right], \quad \varphi_l = \sin^{-1}\left[\frac{\boldsymbol{e}_3^{\mathrm{T}}\bar{\boldsymbol{r}}_{\text{leo},L}}{\left\|\bar{\boldsymbol{r}}_{\text{leo},L}\right\|_2}\right]. \quad (48)$$

The SV position in ENU can also be expressed as

$$\boldsymbol{r}_{\text{leo},l} \triangleq d_l \left[\cos\theta_l \sin\phi_l, \quad \cos\theta_l \cos\phi_l, \quad \sin\theta_l\right]^{\mathrm{T}}. \quad (49)$$

Using coordinate frame transformation, the SV position in ECEF can be obtained from $\boldsymbol{r}_{\text{leo}}$ through

$$\bar{\boldsymbol{r}}_{\text{leo}_l} = \mathbf{R}^{\mathrm{T}}(\varphi_0, \lambda_0)\boldsymbol{r}_{\text{leo},l} + \bar{\boldsymbol{r}}_r \quad (50)$$

where $\bar{\boldsymbol{r}}_r = R_E[\cos\varphi_0 \cos\lambda_0, \cos\varphi_0 \sin\lambda_0, \sin\varphi_0]^{\mathrm{T}}$ is the receiver's position in ECEF and $\mathbf{R}(\varphi_0, \lambda_0)$ is the ECEF to ENU rotation matrix with

$$\mathbf{R}(\varphi_0, \lambda_0) \triangleq \begin{bmatrix} -\sin\lambda_0 & \cos\lambda_0 & 0 \\ -\sin\varphi_0\cos\lambda_0 & -\sin\varphi_0\sin\lambda_0 & \cos\varphi_0 \\ \cos\varphi_0\cos\lambda_0 & \cos\varphi_0\sin\lambda_0 & \sin\varphi_0 \end{bmatrix}.$$

Equation (39) is readily obtained by combining (48)–(50). □

APPENDIX B
DERIVATION OF THE JACOBIAN IN (40)

In the following, the subscripts j and l are omitted for compactness of notation.

$$\text{Define } g_\gamma(\theta) \triangleq \frac{\partial \sin\left[\gamma(\theta)\right]}{\partial\theta} = \left[\frac{\sin\theta}{\alpha\sqrt{1-\frac{\cos^2\theta}{\alpha^2}}} - 1\right]\cos\left[\gamma(\theta)\right]$$

$$g_{01}^{\phi}(\phi,\theta) \triangleq \frac{\partial f_{01}(\phi,\theta)}{\partial\phi} = \sin\lambda_0\sin\phi - \sin\varphi_0\cos\lambda_0\cos\phi$$

$$g_{01}^{\theta}(\phi,\theta) \triangleq \frac{\partial f_{01}(\phi,\theta)}{\partial\theta} = \frac{\cos\varphi_0\cos\lambda_0}{\cos^2\theta}$$

$$g_{02}^{\phi}(\phi,\theta) \triangleq \frac{\partial f_{02}(\phi,\theta)}{\partial\phi} = -\cos\lambda_0\sin\phi - \sin\varphi_0\sin\lambda_0\cos\phi$$

$$g_{02}^{\theta}(\phi,\theta) \triangleq \frac{\partial f_{02}(\phi,\theta)}{\partial\theta} = \frac{\cos\varphi_0\sin\lambda_0}{\cos^2\theta}$$

$$g_{03}^{\phi}(\phi,\theta) \triangleq \frac{\partial f_{03}(\phi,\theta)}{\partial\phi} = \cos\varphi_0\cos\phi$$

$$g_{03}^{\theta}(\phi,\theta) \triangleq \frac{\partial f_{03}(\phi,\theta)}{\partial\theta} = \frac{\sin\varphi_0}{\cos^2\theta}$$

$$b_{01}^{\phi}(\phi,\theta) \triangleq \frac{\partial a_{01}(\phi,\theta)}{\partial\phi} = \sin\left[\gamma(\theta)\right] g_{01}^{\phi}(\phi,\theta)$$

$$b_{01}^{\theta}(\phi,\theta) \triangleq \frac{\partial a_{01}(\phi,\theta)}{\partial\theta} = g_\gamma(\theta) f_{01}(\phi,\theta) + \sin\left[\gamma(\theta)\right] g_{01}^{\theta}(\phi,\theta)$$

$$b_{02}^{\phi}(\phi,\theta) \triangleq \frac{\partial a_{02}(\phi,\theta)}{\partial\phi} = \sin\left[\gamma(\theta)\right] g_{02}^{\phi}(\phi,\theta)$$

$$b_{02}^{\theta}(\phi,\theta) \triangleq \frac{\partial a_{02}(\phi,\theta)}{\partial\theta} = g_\gamma(\theta) f_{02}(\phi,\theta) + \sin\left[\gamma(\theta)\right] g_{02}^{\theta}(\phi,\theta)$$

$$b_{03}^{\phi}(\phi,\theta) \triangleq \frac{\partial a_{03}(\phi,\theta)}{\partial\phi} = \sin\left[\gamma(\theta)\right] g_{03}^{\phi}(\phi,\theta)$$

$$b_{03}^{\theta}(\phi,\theta) \triangleq \frac{\partial a_{03}(\phi,\theta)}{\partial\theta} = g_\gamma(\theta) f_{03}(\phi,\theta) + \sin\left[\gamma(\theta)\right] g_{03}^{\theta}(\phi,\theta).$$

Since by definition $\|\boldsymbol{r}_{\text{leo},l}\|_2 = \alpha R_E$, then the following holds:

$$a_{01}^2(\phi,\theta) + a_{02}^2(\phi,\theta) + a_{03}^2(\phi,\theta) = 1. \quad (51)$$

Subsequently, the elements of the Jacobian matrix $\mathbf{J}_y(\phi,\theta)$ are given by

$$\frac{\partial\lambda}{\partial\phi} \triangleq \frac{b_{02}^{\phi}(\phi,\theta)a_{01}(\phi,\theta) - b_{01}^{\phi}(\phi,\theta)a_{02}(\phi,\theta)}{a_{01}^2(\phi,\theta) + a_{02}^2(\phi,\theta)}$$

$$\frac{\partial\lambda}{\partial\theta} \triangleq \frac{b_{02}^{\theta}(\phi,\theta)a_{01}(\phi,\theta) - b_{01}^{\theta}(\phi,\theta)a_{02}(\phi,\theta)}{a_{01}^2(\phi,\theta) + a_{02}^2(\phi,\theta)}$$

$$\frac{\partial\varphi}{\partial\phi} \triangleq \frac{b_{03}^{\phi}(\phi,\theta)}{\sqrt{a_{01}^2(\phi,\theta) + a_{02}^2(\phi,\theta)}}$$

$$\frac{\partial\varphi}{\partial\theta} \triangleq \frac{b_{03}^{\theta}(\phi,\theta)}{\sqrt{a_{01}^2(\phi,\theta) + a_{02}^2(\phi,\theta)}}$$

and the determinant of $\mathbf{J}_y(\phi,\theta)$ is given by

$$\left|\mathbf{J}_y(\phi,\theta)\right| = \frac{a_{01}\left(b_{02}^{\phi}b_{03}^{\theta} - b_{02}^{\theta}b_{03}^{\phi}\right) - a_{02}\left(b_{01}^{\phi}b_{03}^{\theta} - b_{01}^{\theta}b_{03}^{\phi}\right)}{\left(a_{01}^2 + a_{02}^2\right)^{\frac{3}{2}}}. \quad (52)$$

REFERENCES

[1] T. Reidet al., "Navigation from low Earth orbit–Part 1 Concept, current, capability, and future promise," in *Position, Navigation, and Timing Technologies in the 21st Century*, J. Morton, F. van Diggelen, J. Spilker Jr, and B. Parkinson, Eds., Hoboken, NJ, USA: Wiley, vol. 2, ch. 43, 2021, pp. 1359–1379.

[2] Z. Kassas, "Navigation from low Earth orbit–Part 2: Models, implementation, and performance," in *Position, Navigation, and Timing Technologies in the 21st Century*, J. Morton, F. van Diggelen, J. Spilker Jr, and B. Parkinson, Eds., Hoboken, NJ, USA: Wiley, vol. 2, ch. 43, 2021, pp. 1381–1412.
[3] M. Rabinowitz, "A differential carrier-phase navigation system combining GPS with low earth orbit satellites for rapid resolution of integer cycle ambiguities," Ph.D. dissertation, Stanford Univ., Stanford, CA, USA, 2000.
[4] M. Joerger, L. Gratton, B. Pervan, and C. Cohen, "Analysis of iridium-augmented GPS for floating carrier phase positioning," *J. Inst. Navigation*, vol. 57, no. 2, pp. 137–160, 2010.
[5] M. Joerger, J. Neale, S. Datta-Barua, and B. Pervan, "Ionospheric error modeling for carrier phase-based multiconstellation navigation systems," *IEEE Trans. Aerosp. Electron. Syst.*, vol. 49, no. 1, pp. 451–467, Jan. 2013.
[6] T. Reid, A. Neish, T. Walter, and P. Enge, "Broadband LEO constellations for navigation," *J. Inst. Navigation*, vol. 65, no. 2, pp. 205–220, 2018.
[7] Z. Kassas, J. Morales, and J. Khalife, "New-age satellite-based navigation–STAN: Simultaneous tracking and navigation with LEO satellite signals," *Inside GNSS Mag.*, vol. 14, no. 4, pp. 56–65, 2019.
[8] J. Fischer, "Resilient timekeeping for critical infrastructure," in *Proc. ION Precise Time Interval Syst. Appl. Meeting*, 2020, pp. 234–240.
[9] R. Morales-Ferre, E. Lohan, G. Falco, and E. Falletti, "GDOP-based analysis of suitability of LEO constellations for future satellite-based positioning," in *Proc. IEEE Int. Conf. Wireless Space Extreme Environments*, 2020, pp. 147–152.
[10] Q. Wei, X. Chen, and Y. Zhan, "Exploring implicit pilots for precise estimation of LEO satellite downlink Doppler frequency," *IEEE Commun. Lett.*, vol. 24, no. 10, pp. 2270–2274, Oct. 2020.
[11] D. Racelis and M. Joerger, "Impact of cascading faults on mega-constellation-augmented GNSS PPP integrity," in *Proc. ION GNSS Conf.*, 2020, pp. 3055–3070.
[12] S. Thompson, S. Martin, and D. Bevly, "Single differenced doppler positioning with low earth orbit signals of opportunity and angle of arrival estimation," in *Proc. ION Int. Tech. Meeting Conf.*, 2021, pp. 497–509.
[13] J. Khalife, M. Neinavaie, and Z. Kassas, "Blind doppler tracking from OFDM signals transmitted by broadband LEO satellites," in *Proc. IEEE Veh. Technol. Conf.*, 2021, pp. 1–6.
[14] Z. Kassaset al., "Enter LEO on the GNSS stage: Navigation with starlink satellites," *Inside GNSS Mag.*, vol. 16, no. 6, pp. 42–51, 2021.
[15] R. Sabbagh and Z. Kassas, "Observability analysis of receiver localization via pseudorange measurements from a single LEO satellite," *IEEE Contr. Syst. Lett.*, vol. 7, no. 3, pp. 571–576, 2023.
[16] M. Hartnett, "Performance assessment of navigation using carrier doppler measurements from multiple LEO constellations," Master's thesis, Air Force Inst. Technol., Wright-Patterson AFB, OH, USA, 2022.
[17] M. Jiang, H. Qin, C. Zhao, and G. Sun, "LEO doppler-aided GNSS position estimation," *GPS Solutions*, vol. 26, no. 1, 2022, Art. no. 31.
[18] N. Jardak and Q. Jault, "The potential of LEO satellite-based opportunistic navigation for high dynamic applications," *Sensors*, vol. 22, no. 7, pp. 2541–2565, 2022.
[19] T. Reidet al., "Satellite navigation for the age of autonomy," in *Proc. IEEE/ION Position Location Navigation Symp.*, 2020, pp. 342–352.
[20] A. Nardin, F. Dovis, and J. Fraire, "Empowering the tracking performance of LEO-based positioning by means of meta-signals," *IEEE J. Radio Freq. Identif.*, vol. 5, no. 3, pp. 244–253, Sep. 2021.
[21] J. Khalife and Z. Kassas, "Receiver design for Doppler positioning with LEO satellites," in *Proc. IEEE Int. Conf. Acoust. Speech Signal Process.*, 2019, pp. 5506–5510.
[22] R. Landry, A. Nguyen, H. Rasaee, A. Amrhar, X. Fang, and H. Benzerrouk, "Iridium next LEO satellites as an alternative PNT in GNSS denied environments—Part I," *Inside GNSS Mag.*, vol. 14, no. 3, pp. 56–64, May 2019.
[23] F. Farhangian, H. Benzerrouk, and R. Landry, "Opportunistic in-flight INS alignment using LEO satellites and a rotatory IMU platform," *Aerospace*, vol. 8, no. 10, pp. 280–281, 2021.
[24] A. Elgamoudi, H. Benzerrouk, G. Elango, and R. Landry, "Gauss Hermite H∞ filter for UAV tracking using LEO satellites TDOA/FDOA measurement—Part I," *IEEE Access*, vol. 8, pp. 201428–201 440, 2020.
[25] M. Neinavaie, J. Khalife, and Z. Kassas, "Blind doppler tracking and beacon detection for opportunistic navigation with LEO satellite signals," in *Proc. IEEE Aerosp. Conf.*, 2021, pp. 1–8.
[26] C. Pinell, "Receiver architectures for positioning with low earth orbit satellite signals," Master's thesis, School Electr. Eng., Lulea Univ. Technol., Lulea, Sweden, 2021.
[27] C. Huang, H. Qin, C. Zhao, and H. Liang, "Phase - time method: Accurate Doppler measurement for iridium NEXT signals," *IEEE Trans. Aerosp. Electron. Syst.*, vol. 58, no. 6, pp. 5954–5962, Dec. 2022.
[28] P. Iannucci and T. Humphreys, "Economical fused LEO GNSS," in *Proc. IEEE/ION Position Location Navigation Symp.*, 2020, pp. 426–443.
[29] J. Raquet et al., "Part D: Position, navigation, and timing using radio signals-of-opportunity," in *Position, Navigation, and Timing Technologies in the 21st Century*, J. Morton, F. van Diggelen, J. Spilker Jr, and B. Parkinson, Eds. Hoboken, NJ, USA: Wiley, 2021, vol. 2, ch. 35–43, pp. 1115–1412.
[30] J. McEllroy, J. Raquet, and M. Temple, "Use of a software radio to evaluate signals of opportunity for navigation," in *Proc. ION GNSS Conf.*, 2006, pp. 126–133.
[31] X. Chen, Q. Wei, F. Wang, Z. Jun, S. Wu, and A. Men, "Super-resolution time of arrival estimation for a symbiotic FM radio data system," *IEEE Trans. Broadcast.*, vol. 66, no. 4, pp. 847–856, Dec. 2020.
[32] M. Psiaki and B. Slosman, "Tracking digital FM OFDM signals for the determination of navigation observables," *J. Inst. Navigation*, vol. 69, no. 2, 2022, Art. no. navi.521.
[33] C. Yang and A. Soloviev, "Mobile positioning with signals of opportunity in urban and urban canyon environments," in *Proc. IEEE/ION Position, Location, Navigation Symp.*, 2020, pp. 1043–1059.
[34] N. Souli, P. Kolios, and G. Ellinas, "Online relative positioning of autonomous vehicles using signals of opportunity," *IEEE Trans. Intell. Veh.*, vol. 7, no. 4, pp. 873–885, Dec. 2022, doi: 10.1109/TIV.2021.3124727.
[35] J. Khalife and Z. Kassas, "Navigation with cellular CDMA signals—Part II: Performance analysis and experimental results," *IEEE Trans. Signal Process.*, vol. 66, no. 8, pp. 2204–2218, Apr. 2018.
[36] T. Kang, H. Lee, and J. Seo, "TOA-based ranging method using CRS in LTE signals," *J. Adv. Navigation Technol.*, vol. 23, no. 5, pp. 437–443, Oct. 2019.
[37] P. Wang and Y. Morton, "Multipath estimating delay lock loop for LTE signal TOA estimation in indoor and urban environments," *IEEE Trans. Wireless Commun.*, vol. 19, no. 8, pp. 5518–5530, Aug. 2020.
[38] J. Gante, L. Sousa, and G. Falcao, "Dethroning GPS: Low-power accurate 5 G positioning systems using machine learning," *IEEE Trans. Emerg. Sel. Topics Circuits Syst.*, vol. 10, no. 2, pp. 240–252, Jun. 2020.
[39] H. Dun, C. Tiberius, and G. Janssen, "Positioning in a multipath channel using OFDM signals with carrier phase tracking," *IEEE Access*, vol. 8, pp. 13011–13028, 2020.
[40] K. Shamaei and Z. Kassas, "Receiver design and time of arrival estimation for opportunistic localization with 5G signals," *IEEE Trans. Wireless Commun.*, vol. 20, no. 7, pp. 4716–4731, Jul. 2021.
[41] A. Abdallah and Z. Kassas, "Opportunistic navigation using sub-6 GHz 5G downlink signals: A case study on a ground vehicle," in *Proc. Eur. Conf. Antennas Propag.*, 2022, pp. 1–5.
[42] T. Kazaz, G. Janssen, J. Romme, and A. Van der Veen, "Delay estimation for ranging and localization using multiband channel state information," *IEEE Trans. Wireless Commun.*, vol. 21, no. 4, pp. 2591–2607, Apr. 2022.

[43] I. Lapin, G. Seco-Granados, O. Renaudin, F. Zanier, and L. Ries, "Joint delay and phase discriminator based on ESPRIT for 5G NR positioning," *IEEE Access*, vol. 9, pp. 126550–126563, 2021.
[44] G. Fokin and D. Volgushev, "Software-defined radio network positioning technology design. Problem statement," in *Proc. Syst. Signals Generating Process. Field Board Commun.*, 2022, pp. 1–6.
[45] J. Khalife and Z. Kassas, "On the achievability of submeter-accurate UAV navigation with cellular signals exploiting loose network synchronization," *IEEE Trans. Aerosp. Electron. Syst.*, vol. 58, no. 5, pp. 4261–4278, Oct. 2022.
[46] J. Khalife and Z. Kassas, "Differential framework for submeter-accurate vehicular navigation with cellular signals," *IEEE Trans. Intell. Veh.*, vol. 8, no. 1, pp. 732–744, 2023, doi: 10.1109/TIV.2022.3187957.
[47] D. Vallado and P. Crawford, "SGP4 orbit determination," in *Proc. AIAA/AAS Astrodynamics Specialist Conf. Exhibit*, 2008, pp. 6770–6799.
[48] X. Tian, G. Chen, E. Blasch, K. Pham, and Y. Bar-Shalom, "Comparison of three approximate kinematic models for space object tracking," in *Proc. Int. Conf. Inf. Fusion*, 2013, pp. 1005–1012.
[49] B. Li, J. Huang, Y. Feng, F. Wang, and J. Sang, "A machine learning-based approach for improved orbit predictions of LEO space debris with sparse tracking data from a single station," *IEEE Trans. Aerosp. Electron. Syst.*, vol. 56, no. 6, pp. 4253–4268, Dec. 2020.
[50] H. Benzerrouk, Q. Nguyen, F. Xiaoxing, A. Amrhar, A. Nebylov, and R. Landry, "Alternative PNT based on iridium next LEO satellites Doppler/INS integrated navigation system," in *Proc. Saint Petersburg Int. Conf. Integr. Navigation Syst.*, 2019, pp. 1–10.
[51] Z. Tan, H. Qin, L. Cong, and C. Zhao, "New method for positioning using IRIDIUM satellite signals of opportunity," *IEEE Access*, vol. 7, pp. 83412–83423, 2019.
[52] F. Farhangian and R. Landry, "Multi-constellation software-defined receiver for Doppler positioning with LEO satellites," *Sensors*, vol. 20, no. 20, pp. 5866–5883, Oct. 2020.
[53] M. Orabi, J. Khalife, and Z. Kassas, "Opportunistic navigation with doppler measurements from iridium next and orbcomm LEO satellites," in *Proc. IEEE Aerosp. Conf.*, 2021, pp. 1–9.
[54] H. Geet al., "Initial assessment of precise point positioning with LEO enhanced global navigation satellite systems (LeGNSS)," *Remote Sens.*, vol. 10, no. 7, pp. 984–999, 2018.
[55] B. Li, H. Ge, M. Ge, L. Nie, Y. Shen, and H. Schuh, "LEO enhanced global navigation satellite system (LeGNSS) for real-time precise positioning services," *Adv. Space Res.*, vol. 63, no. 1, pp. 73–93, 2019.
[56] M. Su, X. Su, Q. Zhao, and J. Liu, "BeiDou augmented navigation from low earth orbit satellites," *Sensors*, vol. 19, no. 1, pp. 198–214, 2019.
[57] D. Racelis, B. Pervan, and M. Joerger, "Fault-free integrity analysis of mega-constellation-augmented GNSS," in *Proc. ION GNSS Conf.*, 2019, pp. 465–484.
[58] L. Ye, Y. Yang, X. Jing, L. Deng, and H. Li, "Single-satellite integrated navigation algorithm based on broadband LEO constellation communication links," *Remote Sens.*, vol. 13, no. 4, pp. 703–729, Feb. 2021.
[59] T. Mortlock and Z. Kassas, "Performance analysis of simultaneous tracking and navigation with LEO satellites," in *Proc. ION GNSS Conf.*, 2020, pp. 2416–2429.
[60] S. Kozhaya, J. Haidar-Ahmad, A. Abdallah, Z. Kassas, and S. Saab, "Comparison of neural network architectures for simultaneous tracking and navigation with LEO satellites," in *Proc. ION GNSS Conf.*, 2021, pp. 2507–2520.
[61] N. Khairallah and Z. Kassas, "Ephemeris closed-loop tracking of LEO satellites with pseudorange and Doppler measurements," in *Proc. ION GNSS Conf.*, 2021, pp. 2544–2555.
[62] J. Khalife and Z. Kassas, "Assessment of differential carrier phase measurements from orbcomm LEO satellite signals for opportunistic navigation," in *Proc. ION GNSS Conf.*, 2019, pp. 4053–4063.
[63] J. Khalife, M. Neinavaie, and Z. Kassas, "Navigation with differential carrier phase measurements from megaconstellation LEO satellites," in *Proc. IEEE/ION Position, Location, Navigation Symp.*, 2020, pp. 1393–1404.
[64] K. Pesyna, T. Humphreys, R. Heath, T. Novlan, and J. Zhang, "Exploiting antenna motion for faster initialization of centimeter-accurate GNSS positioning with low-cost antennas," *IEEE Trans. Aerosp. Electron. Syst.*, vol. 53, no. 4, pp. 1597–1613, Aug. 2017.
[65] P. Teunissen, "The least-squares ambiguity decorrelation adjustment: A method for fast GPS integer ambiguity estimation," *J. Geodesy*, vol. 70, no. 1, pp. 65–82, Nov. 1995.
[66] M. Rabinowitz, B. Parkinson, C. Cohen, M. O'Connor, and D. Lawrence, "A system using LEO telecommunication satellites for rapid acquisition of integer cycle ambiguities," in *Proc. IEEE/ION Position Location Navigation Symp.*, 1998, pp. 137–145.
[67] M. Haenggi, J. Andrews, F. Baccelli, O. Dousse, and M. Franceschetti, "Stochastic geometry and random graphs for the analysis and design of wireless networks," *IEEE J. Sel. Areas Commun.*, vol. 27, no. 7, pp. 1029–1046, Sep. 2009.
[68] T. Khan and M. Afshang, "A stochastic geometry approach to Doppler characterization in a LEO satellite network," in *Proc. IEEE Int. Conf. Commun.*, 2020, pp. 1–6.
[69] N. Okati, T. Riihonen, D. Korpi, I. Angervuori, and R. Wichman, "Downlink coverage and rate analysis of low earth orbit satellite constellations using stochastic geometry," *IEEE Trans. Commun.*, vol. 68, no. 8, pp. 5120–5134, Aug. 2020.
[70] A. Talgat, M. Kishk, and M. Alouini, "Stochastic geometry-based analysis of LEO satellite communication systems," *IEEE Commun. Lett.*, vol. 25, no. 8, pp. 2458–2462, Aug. 2021.
[71] D. Jung, J. Ryu. Byun, and J. Choi, "Performance analysis of satellite communication system under the shadowed-Rician fading: A stochastic geometry approach," *IEEE Trans. Commun.*, vol. 70, no. 4, pp. 2707–2721, Apr. 2022.
[72] J. Khalife, M. Neinavaie, and Z. Kassas, "The first carrier phase tracking and positioning results with starlink LEO satellite signals," *IEEE Trans. Aerosp. Electron. Syst.*, vol. 56, no. 2, pp. 1487–1491, Apr. 2022.
[73] Y. Bar-Shalom, T. Kirubarajan, and X. Lin, "Probabilistic data association techniques for target tracking with applications to sonar, radar and EO sensors," *IEEE Aerosp. Electron. Syst. Mag.*, vol. 20, no. 8, pp. 37–56, Aug. 2005.
[74] A. Wrabel, R. Graef, and T. Brosch, "A survey of artificial intelligence approaches for target surveillance with radar sensors," *IEEE Aerosp. Electron. Syst. Mag.*, vol. 36, no. 7, pp. 26–43, Jul. 2021.
[75] P. Misra and P. Enge, *Global Positioning System: Signals, Measurements, and Performance*, 2nd ed. Lincoln, MA, USA: Ganga-Jamuna Press, 2010.
[76] Z. Kassas and T. Humphreys, "Observability analysis of collaborative opportunistic navigation with pseudorange measurements," *IEEE Trans. Intell. Transp. Syst.*, vol. 15, no. 1, pp. 260–273, Feb. 2014.
[77] Y. Bar-Shalom, X. Li, and T. Kirubarajan, *Estimation With Applications to Tracking and Navigation*. Hoboken, NJ, USA: Wiley, 2002.
[78] SpaceX, "FCC file number: SATMOD2018110800083," *IB FCC Rep.*, Nov. 2018. [Online]. Available: https://licensing.fcc.gov/cgi-bin/ws.exe/prod/ib/forms/attachment_menu.hts?id_app_num=128513&acct=599269&id_form_num=15&filing_key=-425955
[79] G. Casella, C. Robert, and M. Wells, "Generalized accept-reject sampling schemes," *Lecture Notes-Monograph Ser.*, vol. 45, pp. 342–347, 2004.
[80] J. Vetter, "Fifty years of orbit determination: Development of modern astrodynamics methods," *Johns Hopkins APL Tech. Dig.*, vol. 27, no. 3, pp. 239–252, Nov. 2007.
[81] J. Khalife and Z. Kassas, "Opportunistic UAV navigation with carrier phase measurements from asynchronous cellular signals," *IEEE Trans. Aerosp. Electron. Syst.*, vol. 56, no. 4, pp. 3285–3301, Aug. 2020.

[82] J. Morales, J. Khalife, and Z. Kassas, "Information fusion strategies for collaborative inertial radio SLAM," *IEEE Trans. Intell. Transp. Syst.*, vol. 23, no. 8, pp. 12935–12952, Aug. 2022.

Joe Khalife (Member, IEEE) received the B.E. degree in electrical engineering and the M.S. degree in computer engineering from the Lebanese American University (LAU), Beirut, Lebanon, in 2011 and 2014, and the Ph.D. degree in electrical engineering and computer science from the University of California, Irvine, CA, USA, in 2020.

He was a Postdoctoral Fellow with the University of California and member of the Autonomous Systems Perception, Intelligence, and Navigation (ASPIN) Laboratory. From 2012 to 2015, he was a Research Assistant with LAU, and has been a member of the ASPIN Laboratory, since 2015. His research interests include opportunistic navigation, autonomous vehicles, and software-defined radio.

Dr. Khalife was the recipient of the 2016 IEEE/ION Position, Location, and Navigation Symposium (PLANS) Best Student Paper Award, 2018 IEEE Walter Fried Award, and 2021 IEEE AESS Robert T. Hill Best Dissertation Award.

Zaher (Zak) M. Kassas (Senior Member, IEEE) received the B.E. degree in electrical engineering from the Lebanese American University, Beirut, Lebanon, the M.S. degree in electrical and computer engineering from The Ohio State University, Columbus, OH, USA, the M.S.E. degree in aerospace engineering and the Ph.D. in electrical and computer engineering from the University of Texas at Austin, Austin, TX, USA.

He is currently a Professor of Electrical and Computer Engineering with The Ohio State University and Director of the Autonomous Systems Perception, Intelligence, and Navigation (ASPIN) Laboratory. He is also the Director of the U.S. Department of Transportation Center: CARMEN (Center for Automated Vehicle Research with Multimodal AssurEd Navigation), Ohio State University, focusing on navigation resiliency and security of highly automated transportation systems. His research interests include cyber-physical systems, estimation theory, navigation systems, autonomous vehicles, and intelligent transportation systems.

Dr. Kassas was the recipient of the 2018 National Science Foundation CAREER Award, 2019 Office of Naval Research Young Investigator Program Award, 2022 Air Force Office of Scientific Research YIP Award, 2018 IEEE Walter Fried Award, 2018 Institute of Navigation (ION) Samuel Burka Award, and 2019 ION Col. Thomas Thurlow Award. He is an Associate Editor for IEEE TRANSACTIONS ON AEROSPACE AND ELECTRONIC SYSTEMS and IEEE TRANSACTIONS ON INTELLIGENT TRANSPORTATION SYSTEMS. He is a Distinguished Lecturer of the IEEE Aerospace and Electronic Systems Society.